Small

NANO · MICRO small
www.small-journal.com

RESEARCH ARTICLE

Generation of a Built-In Electric Field in the Heterostructure MoS_2/Ni3Se_2 Facilitates Hydrogen Production via Energy-Saving Urea Oxidation

Boka Fikadu Banti[1] | Hyojin Kang[2] | Indra Memdi Khoris[3] | Cheru Fekadu Molla[1] | Birhanu Bayissa Gicha[4] | Jihyeon Yeom[4] | Njemuwa Nwaji[5] | Jaebeom Lee[1,3,6]

[1]Department of Chemistry, Chungnam National University, Daejeon, Republic of Korea | [2]Institute For Sciences of the Universe, Chungnam National University, Daejeon, Republic of Korea | [3]Research Institute of Materials Chemistry, Chungnam National University, Daejeon, Republic of Korea | [4]Department of Materials Science and Engineering, Korea Advanced Institute of Science and Technology (KAIST), Daejeon, Republic of Korea | [5]Institute of Fundamental Technological Research, Polish Academy of Sciences, Warsaw, Poland | [6]SpinPlas Solution Inc., Daejeon, Republic of Korea

Correspondence: Njemuwa Nwaji (nnwaji@ippt.pan.pl) | Jaebeom Lee (nanoleelab@cnu.ac.kr)

Received: 25 June 2026 | **Revised:** 28 July 2026 | **Accepted:** 7 August 2026

Keywords: built-in electric field | electrocatalysis | hydrogen production | MoS_2/Ni_3Se_2 heterostructure | urea oxidation reaction

ABSTRACT

The urea oxidation reaction (UOR) offers a sustainable and thermodynamically favorable alternative to the oxygen evolution reaction, enabling coupling of urea-rich wastewater remediation with energy-efficient hydrogen production. However, the sluggish six-electron-transfer kinetics of UOR necessitate advanced electrocatalysts to accelerate reaction dynamics. Heterostructure engineering provides an effective strategy to regulate interfacial charge redistribution and enhance catalytic activity. Herein, we report a rationally designed MoS_2/Ni_3Se_2 heterostructure with an intrinsic built-in electric field, constructed on nickel foam via hydrothermal growth followed by electrodeposition, exhibiting efficient bifunctional electrocatalytic activity toward UOR and the hydrogen evolution reaction. Density functional theory calculations reveal spontaneous interfacial charge transfer at the MoS_2/Ni_3Se_2 interface, generating localized electrophilic and nucleophilic regions that facilitate urea adsorption, promote bond activation, and accelerate decomposition kinetics. Benefiting from this interfacial electronic modulation, the catalyst requires only 1.20 V vs. RHE to achieve 10 mA cm^{-2} for UOR in 1 M KOH + 0.5 M urea and an overpotential of 81 mV to reach the same current density for HER in 1 M KOH. Furthermore, the assembled UOR//HER electrolyzer operates at 1.31 V at 10 mA cm^{-2} and maintains stable performance for over 100 h. This work advances heterostructure-based urea-assisted hydrogen production for sustainable electrocatalysis.

1 | Introduction

Rising concerns over energy scarcity and environmental degradation have driven extensive efforts to develop efficient and sustainable technologies for clean energy conversion [1–3]. Among these, water electrolysis has emerged as a promising route for green hydrogen production due to its zero-carbon emissions and environmental compatibility [4, 5]. Nevertheless, its overall efficiency is fundamentally limited by the sluggish oxygen evolution reaction (OER), which requires a substantial anodic overpotential. To address this limitation, considerable attention has been directed toward replacing the OER with more thermodynamically favorable organic oxidation reactions, including alcohols, aldehydes, hydrazine, and urea, to achieve energy-efficient hydrogen production [6–9]. Among these alternatives, UOR is particularly attractive due to its abundance, low

cost, environmental compatibility, and low oxidation potential. Notably, the thermodynamic potential of the UOR (0.37 V vs. RHE) is substantially lower than that of the OER (1.23 V vs. RHE), allowing electrolysis at reduced energy input and improved energy-conversion efficiency [10–12]. In addition, UOR offers a dual benefit by enabling the remediation of urea-containing wastewater, thereby enhancing both environmental and practical value [13–15].

Despite these advantages, the practical implementation of UOR remains challenging due to the intrinsically sluggish six-electron transfer kinetics and the strong C—N bond in urea molecules [16, 17]. Ni-based catalysts have been widely recognized as highly active UOR electrocatalysts because Ni species can effectively facilitate C—N bond dissociation. Nevertheless, the catalytic activity and selectivity are often limited by insufficient control of interfacial charge distribution and competing adsorption of hydroxyl species in alkaline media. In this context, heterostructure engineering has emerged as an effective strategy to modulate interfacial electronic structures and promote catalytic reactions. Recent advances in heterostructure engineering, crystallinity modulation, and 2D materials further underscore the pivotal role of interfacial electronic-structure regulation in accelerating hydrogen evolution and charge-transfer kinetics across diverse catalytic systems [18–20]. For instance, in Ni-modified Co_2VO_4 heterojunctions, electron transfer from Ni to Co_2VO_4 generates high-valent NiOOH and electron-rich Co_2VO_4, enabling selective adsorption of urea's C═O on Co_2VO_4 and -NH_2 on NiOOH, creating opposing electronic pulls that facilitate C—N bond cleavage [21]. Notably, interfacial charge redistribution within heterojunctions lowers the Gibbs free energy for NiOOH formation, pinpointing these sites as the true active centers for UOR. Heterostructures such as $NiSe_2/MoSe_2$ [22] and NiF_3/Ni_2P [23] exhibit markedly reduced pre-oxidation potentials relative to their single-phase analogues, a consequence of interfacial electron modulation.

In alkaline media, UOR proceeds through multiple proton-coupled electron-transfer steps involving C—N bond cleavage. However, excessive adsorption of OH^- species on catalyst surfaces can compete with urea adsorption and promote the undesired OER pathway. Notably, urea molecules contain both electron-donating amino (—NH_2) and electron-withdrawing carbonyl (C═O) groups, providing opportunities for selective adsorption on catalytically differentiated sites. Recent studies show that heterojunctions comprising components with distinct energy levels spontaneously generate built-in electric fields and stable local electrophilic/nucleophilic sites at the interface, thereby enhancing electronic migration and promoting selective adsorption of electron-donating or -withdrawing moieties in urea [24]. For example, Yan et al. demonstrated that $CoS_{1.097}/Ni_3S_2$ heterojunctions exhibit enhanced UOR activity, attributed to self-driven interfacial electron flow between the constituent phases, which establishes oppositely charged regions that facilitate urea adsorption and activation [25]. Jiao and colleagues demonstrated that —NH_2 and C═O groups preferentially adsorb on Ni_3N and Mo_2N, respectively, while the Ni_3N/Mo_2N heterostructure synergistically combines the merits of the individual phases, thereby enhancing urea adsorption [26]. These advances motivate the rational design of Ni-based systems that concurrently suppress self-oxidation and enhance urea adsorption, aiming to achieve highly selective UOR catalysts with outstanding activity and stability at industrially relevant current densities, yet this remains a formidable challenge.

Inspired by these considerations, we constructed a MoS_2/Ni_3Se_2 heterostructure, and the work function mismatch between MoS_2 and Ni_3Se_2 in the heterostructure electrocatalyst induces an intrinsic built-in electric field that facilitates urea-assisted hydrogen generation. The heterointerface between MoS_2 and Ni_3Se_2 induces energy-level alignment and interfacial band reconstruction, generating an internal electric field that facilitates directional charge migration. In situ Raman spectroscopy reveals that this structure effectively regulates catalyst self-oxidation and suppresses excessive NiOOH accumulation during UOR. Density functional theory (DFT) calculations further reveal that spontaneous electron migration from Ni_3Se_2 to MoS_2 generates electrophilic Ni_3Se_2 sites and nucleophilic MoS_2 sites, which preferentially interact with the electron-donating —NH_2 and electron-withdrawing C═O groups of urea, respectively. This interfacial charge redistribution promotes urea adsorption while limiting excessive OH^- accumulation, thereby favoring UOR over the competing OER pathway. As a result, the MoS_2/Ni_3Se_2 heterostructure exhibits highly selective and efficient UOR activity. These results deliver key insight into the interfacial engineering of heterostructured electrocatalysts and establish an effective strategy for achieving energy-efficient hydrogen production via urea-assisted electrolysis.

2 | Results and Discussion

2.1 | Interfacial Electric-Field–Mediated Catalysis in a MoS_2/Ni_3Se_2 Heterostructure

We envisaged that the semiconducting nature of MoS_2 and the metallic behavior of Ni_3Se_2 would fundamentally influence electron distribution at their interface when assembled into a heterostructure, thereby significantly enhancing catalytic performance in urea-assisted water electrolysis. To test this hypothesis, DFT calculations were performed to elucidate the built-in electric field (BIEF) effect in the MoS_2/Ni_3Se_2 heterointerface during urea oxidation. Figure 1a presents a conceptual model illustrating the origin of charge redistribution at the MoS_2/Ni_3Se_2 interface. According to band theory, the work-function difference governs electron transfer across the heterointerface. As shown in Figure 1b,c, the work function of MoS_2 (5.41 eV) is higher than that of Ni_3Se_2 (5.12 eV), indicating a clear work-function mismatch between the two components. Upon contact, the electrochemical potential difference drives electron transfer from Ni_3Se_2 to MoS_2 until Fermi-level equilibration is reached, generating an interfacial electric field. This charge redistribution results in electron enrichment on MoS_2 and hole accumulation on Ni_3Se_2, thereby establishing a BIEF at the heterointerface. The resulting asymmetric charge distribution also creates an intrinsic interfacial polarity, in which the electron-rich MoS_2 and electron-deficient Ni_3Se_2 generate a directional electrostatic potential that facilitates charge separation and promotes electron transport across the heterointerface while suppressing charge recombination.

Charge-density-difference analysis further confirms pronounced interfacial charge redistribution in the MoS_2/Ni_3Se_2

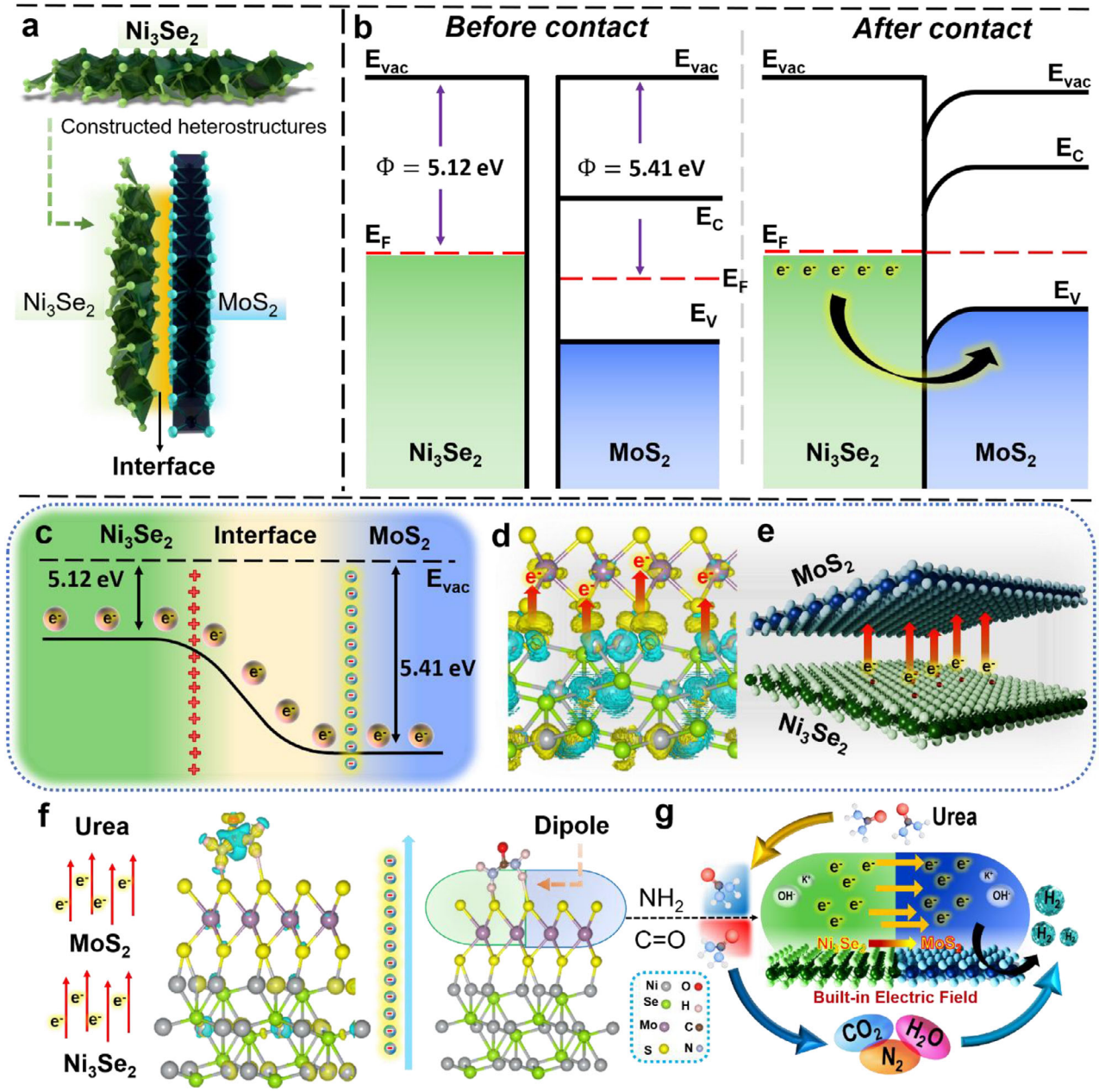

FIGURE 1 | Structural evolution and electronic modulation of the MoS_2/Ni_3Se_2 heterostructure. (a) Schematic representation of interfacial charge redistribution across the MoS_2/Ni_3Se_2 heterostructure interface. (b) Work-function alignment of MoS_2 and Ni_3Se_2 before and after contact. (c) Formation of the BIEF at the heterojunction. (d) Charge-density-difference distribution of the MoS_2/Ni_3Se_2 heterostructure. (e) Interfacial charge transfer across the MoS_2/Ni_3Se_2 interface. (f) Schematic illustration of the adsorption configuration and electrocatalytic pathway for urea oxidation on the MoS_2/Ni_3Se_2 heterostructure. (g) Interfacial activation of urea molecules at the MoS_2/Ni_3Se_2 heterointerface.

heterostructure. As shown in Figure 1d, electron accumulation (yellow) occurs on the MoS_2 side, whereas electron depletion (blue) appears on Ni_3Se_2, evidencing the formation of a built-in electric field across the heterointerface. This polarized interface provides a continuous driving force for electron migration across the heterointerface toward the catalytically active surface, thereby enhancing interfacial charge-transfer kinetics during urea oxidation. The redistribution of interfacial electrons induces upward electron migration toward the surface, facilitating efficient urea oxidation (Figure 1e). The electron-rich MoS_2 surface strengthens the interaction with urea molecules, enhancing their adsorption at the catalytic interface and facilitating subsequent oxidation steps (Figure 1f). Consequently, the heterointerface enriches urea molecules and electronically modulates the active sites, facilitating C—N bond activation and accelerating the kinetics of urea electrooxidation (Figure 1g).

2.2 | Synthesis and Morphological Characterization of MoS_2/Ni_3Se_2 Heterostructure

Based on the above prediction, the MoS_2/Ni_3Se_2 heterostructured catalyst was rationally constructed via a hydrothermal approach followed by electrodeposition, as schematically

illustrated in Figure 2a. Specifically, Ni_3Se_2 nanorods were grown directly on nickel foam using a hydrothermal method, with the substrate serving as both the Ni source and a conductive scaffold. $NaBH_4$ induced the release of Ni ions from the foam surface, thereby driving the in situ formation of the Ni_3Se_2 nanoarrays. The nanorods form a uniformly aligned architecture with strong substrate integration and robust mechanical stability. Subsequently, MoS_2 nanosheets were directly anchored onto the Ni_3Se_2 nanorod arrays via a facile potentiostatic electrodeposition process, using ammonium tetrathiomolybdate as the Mo and S precursor, thereby forming the MoS_2/Ni_3Se_2 heterostructure. For comparison, individual MoS_2 counterparts were synthesized under identical conditions. The morphological features of Ni_3Se_2, MoS_2, and the MoS_2/Ni_3Se_2 heterostructure were systematically investigated using scanning electron microscopy (SEM) and transmission electron microscopy (TEM) to elucidate their structural characteristics. The low and high-magnification SEM images (Figure 2b,c) and TEM images (Figure 2f; Figure S1) of Ni_3Se_2 reveal vertically aligned smooth nanorods uniformly anchored to the NF substrate, forming a well-defined hierarchical architecture. Energy-dispersive X-ray spectroscopy (EDX) elemental mapping indicates a uniform distribution of Ni and Se within the whole Ni_3Se_2 phase, corroborating the successful formation of phase-pure Ni_3Se_2 (Figure S1). After electrodeposition, the SEM image shows a hierarchical MoS_2 with a roughened surface that was intimately grown on the surface of the Ni_3Se_2 (Figure 2d, e). The TEM image of the hybrid MoS_2/Ni_3Se_2 clearly shows a Ni_3Se_2 core and MoS_2 shell (Figure 2g). In the absence of the freestanding Ni_3Se_2 nanorod, electrodeposition only yields MoS_2 nanosheets, indicating that the Ni_3Se_2 guided the vertical growth of MoS_2 on the NF substrate (Figure S2). It is pertinent to note that electrodeposition after one and two cycles formed insufficient coverage of the nanorods (Figure S3), while four and five-cycle deposition shows aggregation (Figure S4), which prevents fast electrolyte flow and reduces performance, as will be discussed later. Thus, three-cycle electrodeposition yields the optimal performance. Furthermore, a room-temperature growth of MoS_2 on the Ni_3Se_2 was explored, but irregular and aggregated MoS_2 were also visible outside the nanorods (Figure S5), which reduces the electrocatalytic ability, as will be discussed, suggesting that electrochemical deposition is a more beneficial strategy. The ultrathin nanosheets uniformly coating the nanorod array both maximize exposure of active sites for enhanced electrolyte access and provide ample open space to accelerate mass transport of reactants, urea-derived intermediates, and gaseous products during the UOR [27, 28]. To investigate the interplanar distances of MoS_2/Ni_3Se_2, a fast Fourier transform (FFT) and its inverse FFT were executed in the selected regions of the HRTEM (Figure 3a) using Gatan Digital Micrograph software. HR-TEM reveals a well-defined, continuous interface between MoS_2 and Ni_3Se_2, directly confirming the successful formation of the heterostructure. The observed lattice fringe spacing of 0.165 nm is assigned to the (110) plane of Ni_3Se_2, while the ordered fringes of 0.276 nm correspond to the (100) plane of MoS_2. The MoS_2/Ni_3Se_2 interface facilitates interfacial charge redistribution, generating a stable local electrophilic/nucleophilic environment that selectively adsorbs the electron-donating ($-NH_2$) and electron-withdrawing ($-C=O$) groups of urea, thereby accelerating its cleavage and delivering outstanding UOR performance [29]. EDX elemental mapping demonstrates a highly uniform dispersion of the predominant existence of Se and Ni in the core, while Mo and S dominate the shell of the nanorods, evidencing the successful formation of the MoS_2/Ni_3Se_2 interface (Figure 2h).

Powder X-ray diffraction (XRD) analysis (Figure 3b; Figure S6) was conducted to elucidate the crystallographic structure of the as-prepared electrocatalyst. The XRD of MoS_2 exhibits diffraction peaks observed at 2θ = 14.5°, 33.0°, 39.3°, 58.5°, and 69.7°, which can be unambiguously assigned to the (002), (100), (103), (110), and (201) planes of pure hexagonal MoS_2 phase (JCPDS card no.371492), as previously reported [30, 31]. Likewise, the prominent peaks that correspond to the (101), (110), (003), (202), (300), and (024) planes of Ni_3Se_2 (JCPDS No.19-0841) can be clearly seen at 2θ = 20.94°, 29.52°, 37.15°, 42.55°, 52.45°and 62.29°. The XRD of the hybrid MoS_2/Ni_3Se_2 showed distinct peaks for both Ni_3Se_2 and MoS_2, indicating the successful formation of a heterostructure.

Given that the oxidation state of metal centers plays a decisive role in governing electrocatalytic activity, X-ray photoelectron spectroscopy (XPS) was employed to probe the chemical valence states and electronic environments within the MoS_2/Ni_3Se_2 heterostructure. The XPS survey spectra confirm the presence of all expected constituent elements, each appearing at its characteristic binding energy position (Figure S7). The XPS deconvolution of the Ni 2p in MoS_2/Ni_3Se_2 shows distinct peaks at 856.11 and 873.39 eV (Figure 3c), attributed to the spin-orbit doublet of Ni $2p_{3/2}$ and Ni $2p_{1/2}$ orbitals in Ni^{2+} [32]. The observed satellite peaks located at 856.89 and 875.10 eV suggest the presence of the Ni^{3+} ion [33]. Compared to pure Ni_3Se_2, the Ni 2p binding energy reveals a positive shift of 0.3 eV, indicating the occurrence of an electron transfer process. Moreover, the Ni_3Se_2 sample shows a weak peak at a binding energy of 853.1 eV, indicating the existence of metallic Ni^0 in the material. The deconvoluted Mo 3d (Figure 3d) reveals a pair of peaks at 226.8 and 229.01 eV, which correspond to the S species bonded to the Mo ion [34]. The two distinct binding energy signals at 232.02 and 234.91 eV are consistent with the Mo $3d_{5/2}$ and Mo $3d_{3/2}$ orbitals, respectively [35]. The Mo 3d in the hybrid MoS_2/Ni_3Se_2 shows a negative shift of 0.35 eV relative to that of pure MoS_2. The positive shift for Ni 2p and negative shift for Mo 3d in MoS_2/Ni_3Se_2 indicates that electrons are transferred from Ni_3Se_2 to MoS_2 across the heterointerface, which agrees with the DFT result and confirms the existence of charge redistribution. The Se 3d deconvolution in MoS_2/Ni_3Se_2 reveals the spin-orbit doublet at 54.21 and 55.45 eV (Figure 3e) that can be assigned to Se $3d_{5/2}$ and Se $3d_{3/2,}$ respectively. The Se 3d in Ni_3Se_2 shows a negative shift of 0.5 eV relative to that of MoS_2/Ni_3Se_2. The observed broader peak centered around 58.5 eV can be attributed to oxidized selenium species (SeO_x), which probably originated from surface oxidation [36].

Given the critical role of surface accessibility in electrocatalysis, the textural properties of the materials were investigated by N_2 adsorption–desorption analysis. Brunauer–Emmett–Teller (BET) measurements revealed the specific surface areas and pore size distributions of the samples (Figure S8). All samples exhibit characteristic type IV adsorption–desorption isotherms with pronounced H3 hysteresis loops, consistent with the presence of well-developed mesoporous structures. Anchoring intrinsically microporous MoS_2 onto Ni_3Se_2 induces the formation of supplementary mesopores, producing a MoS_2/Ni_3Se_2 heterostructure with a BET surface area of 42.14 $m^2\ g^{-1}$, which exceeds those of

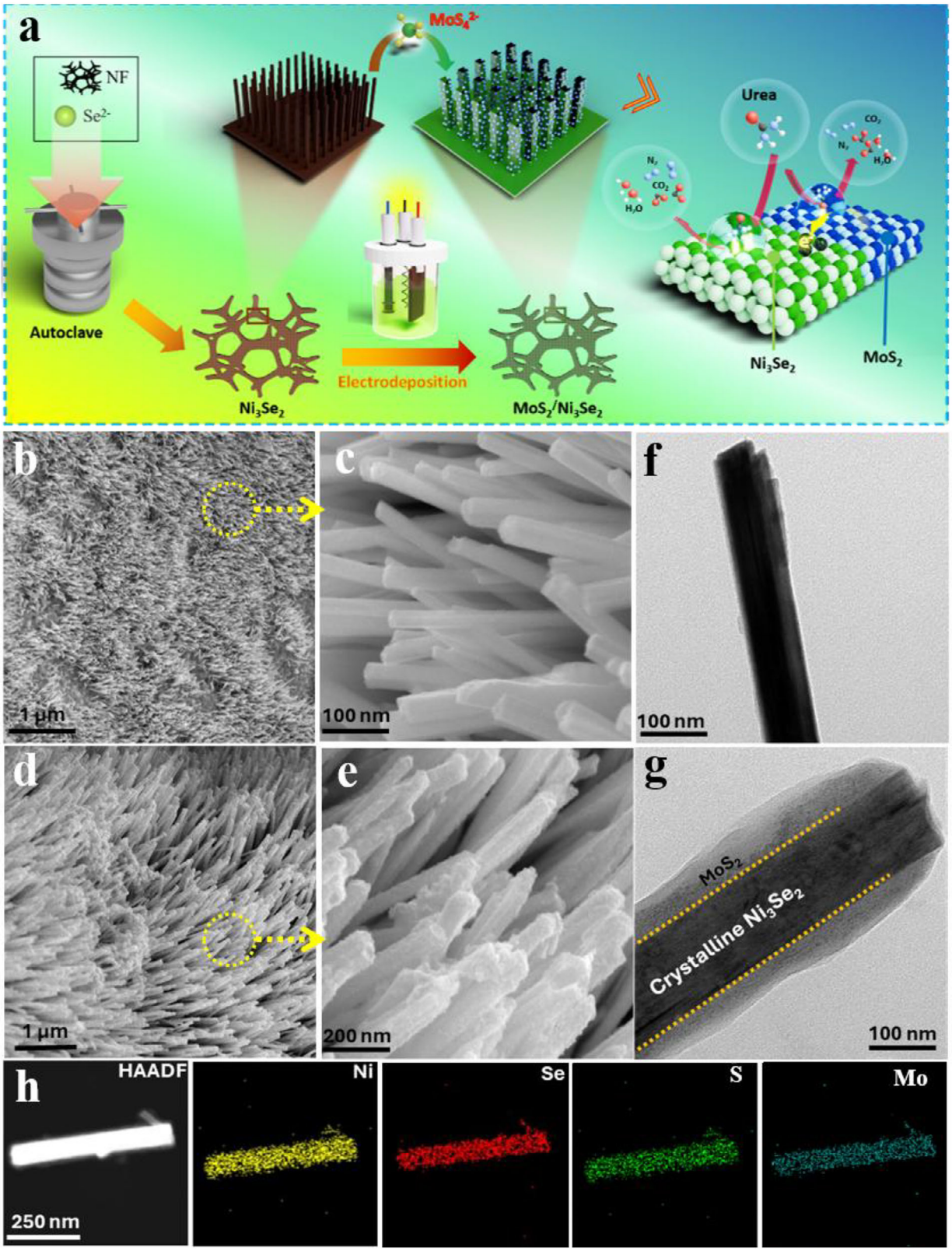

FIGURE 2 | Construction and morphological characterization of the MoS_2/Ni_3Se_2 heterostructure. (a) Schematic overview of the stepwise fabrication of the MoS_2/Ni_3Se_2 heterostructure catalyst. SEM images of (b, c) Ni_3Se_2 and (d, e) MoS_2/Ni_3Se_2. TEM images of (f) Ni_3Se_2 and (g) MoS_2/Ni_3Se_2. (h) HAADF-STEM characterization combined with elemental mapping confirms the uniform dispersion of Mo, S, Ni, and Se across the MoS_2/Ni_3Se_2 heterostructure, indicating the successful integration of the two components.

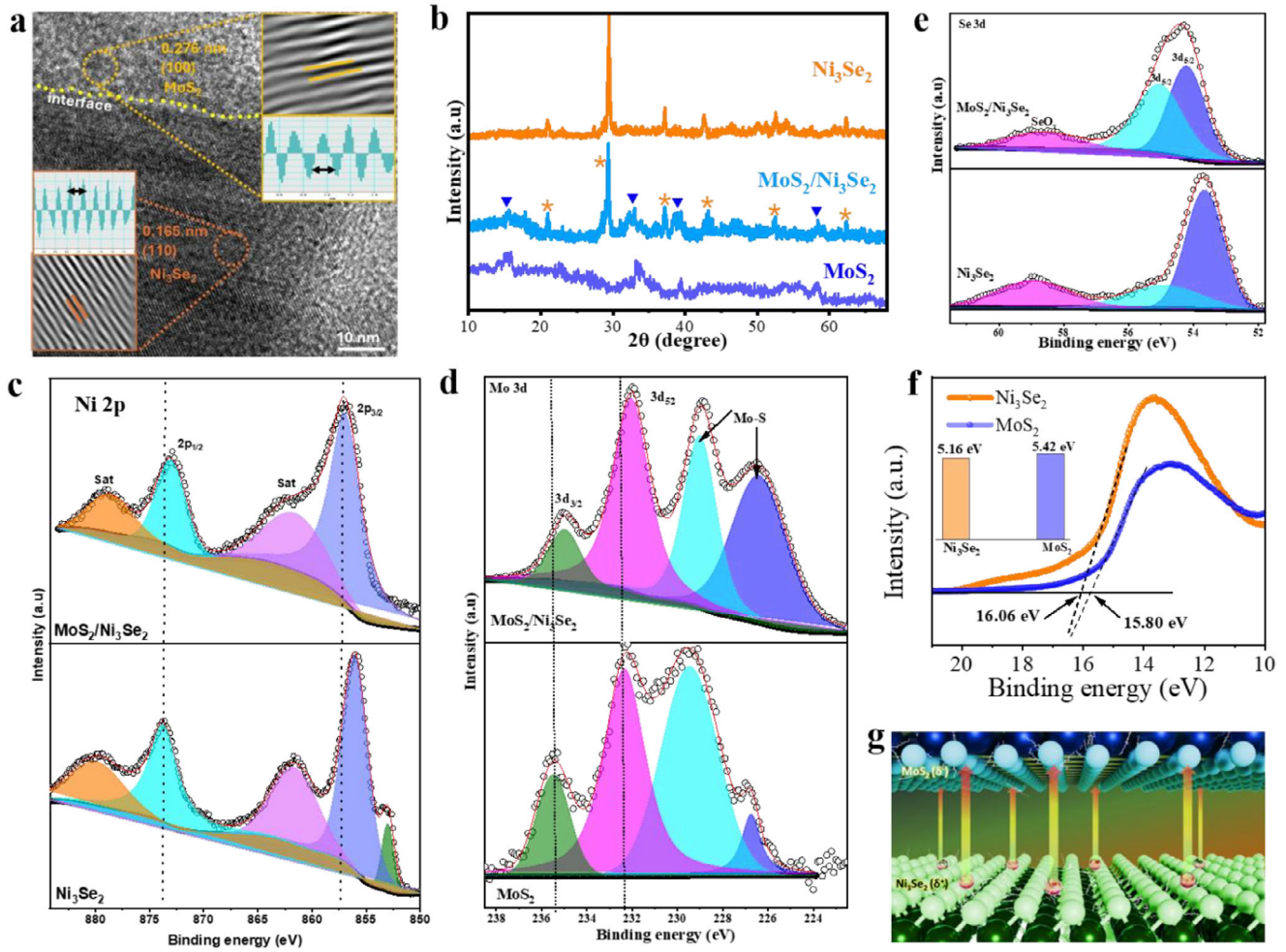

FIGURE 3 | Crystallographic and structural characterization of the MoS_2, Ni_3Se_2, and MoS_2/Ni_3Se_2 heterostructure. (a) HR-TEM image of MoS_2/Ni_3Se_2. (b) XRD of MoS_2, Ni_3Se_2, and MoS_2/Ni_3Se_2 catalysts. XPS spectra of (c) Ni 2p, (d) Mo 3d, and (e) Se 3d. (f) UPS characterization of MoS_2 and Ni_3Se_2, indicating their corresponding work functions. (g) Schematic representation of the interfacial electron transfer process between MoS_2 and Ni_3Se_2.

individual MoS_2 (39.32 $m^2\ g^{-1}$) and Ni_3Se_2 (36.76 $m^2\ g^{-1}$). The enlarged surface area and pore size induced by heterointerface formation highlight the effectiveness of interface engineering in concurrently regulating electronic properties and enhancing surface accessibility.

The effectiveness of interfacial charge transport is governed by the ease of electron extraction, which can be quantitatively evaluated through the work function. The work functions of MoS_2 (5.42 eV) and Ni_3Se_2 (5.16 eV) were obtained from ultraviolet photoelectron spectroscopy (UPS) measurements (Figure 3f) using the relation work function = 21.22 – (E_{cutoff} − E_F) [37, 38], where 21.22 eV corresponds to the incident photon energy, E_{cutoff} denotes the secondary electron cutoff, and E_F is the Fermi level. The lower work function of Ni_3Se_2 raises its Fermi level relative to that of MoS_2, thereby driving spontaneous interfacial charge transfer from Ni_3Se_2 to MoS_2 and establishing a stable built-in electric field (BIEF) at the interface (Figure 3g). The proposed BIEF is further supported by the consistent agreement among the UPS-derived work-function difference, the XPS binding-energy shifts, and the DFT-calculated charge-density-difference analysis, collectively indicating spontaneous interfacial electron transfer and charge redistribution across the MoS_2/Ni_3Se_2 heterointerface.

To uncover the microscopic origin of the improved electrocatalytic performance, conductive atomic force microscopy (c-AFM) measurements were carried out in ambient, dry conditions under an applied bias (Figure 4a). Atomic force microscopy (AFM) analysis and the corresponding height profile along the red dashed line in Figure 4b reveal a Ni_3Se_2 nanorod array with a maximum height of ~62.72 nm (Figure 4b, c). Similarly, AFM imaging and height profiling along the red dashed line in Figure 4c confirm the formation of a MoS_2/Ni_3Se_2 heterostructure with a maximum thickness of ~91.97 nm (Figure 4d,e). The Z-height current maps acquired under a DC bias (Figure 4f,k) reveal conductivity variations that are closely correlated with surface topography, with MoS_2/Ni_3Se_2 exhibiting a more spatially homogeneous and broadly distributed current response across the scanned area. The spatially resolved current distributions acquired under positive (Figure 4g,l) and negative (Figure 4h,m) bias reveal markedly different charge-transport characteristics across the investigated materials. Ni_3Se_2 exhibits spatially discrete, bias-dependent conductive domains, whereas the MoS_2/Ni_3Se_2 heterostructure

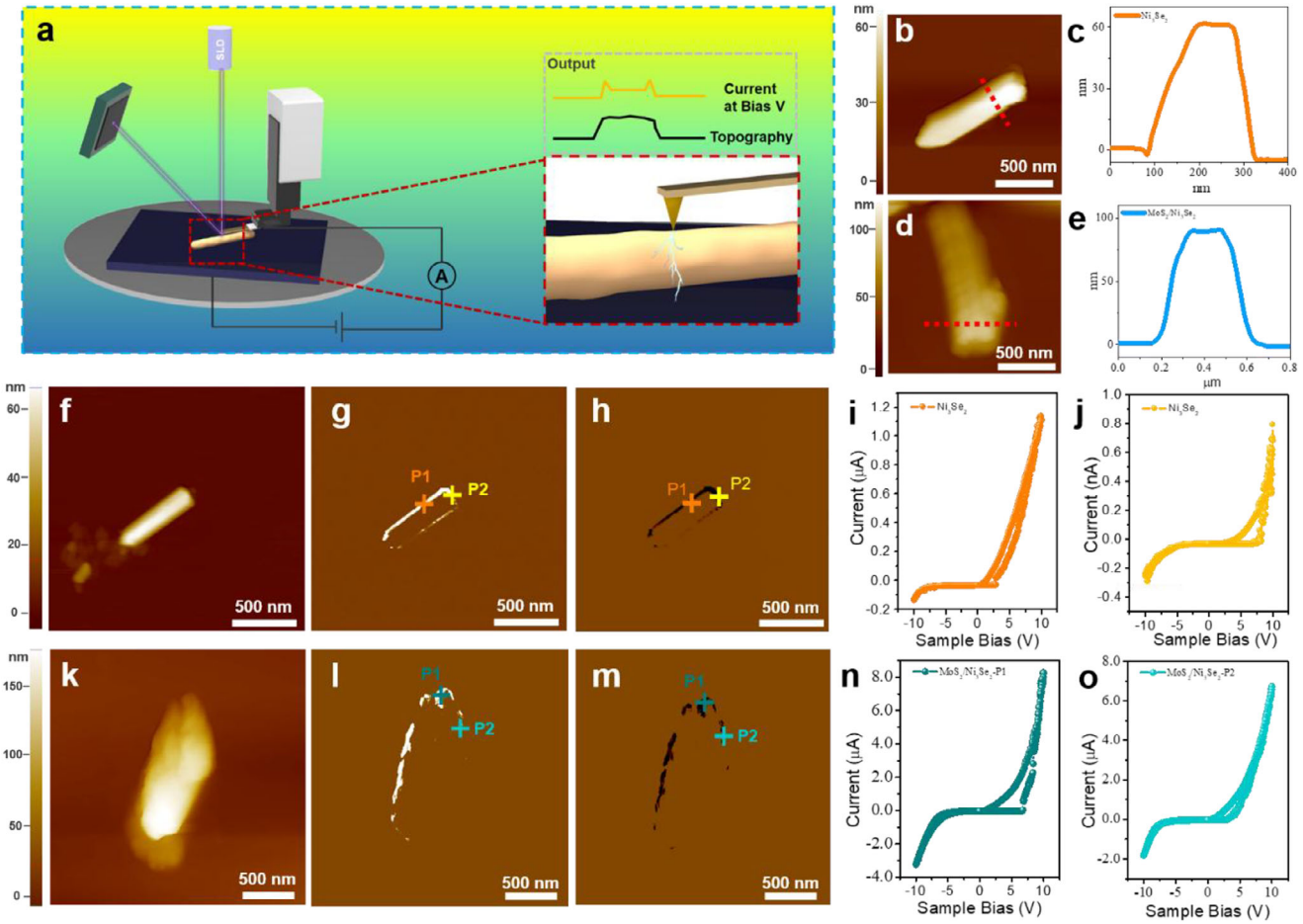

FIGURE 4 | AFM and c-AFM analysis. (a) Schematic representation of the c-AFM measurement configuration. (b) AFM image, (c) corresponding height profile along the red dashed line in (b), revealing a Ni_3Se_2 nanorod with a maximum height of ~62.72 nm. (d) AFM image, (e) corresponding height profile along the red dashed line in (d), revealing a MoS_2/Ni_3Se_2 heterostructure with a maximum height of ~91.97 nm. (f,k) Z-height current images, (g,l) corresponding current maps under forward bias, and (h,m) under reverse bias. (i,n) and (j,o) *I–V* curves recorded at selected points (P1, P2) on Ni_3Se_2 and MoS_2/Ni_3Se_2 heterostructure, respectively.

displays a markedly more uniform current landscape, reflecting the formation of an efficient and continuous interfacial charge-transport network induced by MoS_2 integration. Consistently, current–voltage (*I–V*) measurements acquired at representative locations reveal that, compared with pristine Ni_3Se_2 (Figure 4i,j), the MoS_2/Ni_3Se_2 heterostructure (Figure 4n,o) exhibits markedly steeper and more symmetric *I–V* responses. These features indicate more efficient charge injection at the local junctions and a pronounced suppression of hysteretic behavior. The enhanced local current response and improved charge injection observed by c-AFM indicate superior interfacial conductivity within the heterostructure, providing microscopic evidence for the accelerated electron-transport pathways that facilitate the subsequent electrochemical charge-transfer process.

2.3 | Electrocatalytic Performance Evaluation for the HER

To reveal the structural benefits of MoS_2/Ni_3Se_2 heterostructures for HER, we systematically assessed the electrocatalytic activity of NF, MoS_2, Ni_3Se_2, Pt/C, and MoS_2/Ni_3Se_2 in 1.0 M KOH using a standard three-electrode setup. The linear sweep voltammetry (LSV) for Ni_3Se_2 nanorods and different MoS_2 depositions is shown in Figure S9. We observed better catalytic performance with three-cycle depositions; hence, it was selected for further study. The HER LSV profiles (Figure 5a) reveal that the MoS_2/Ni_3Se_2 heterostructure delivers exceptional HER performance, reaching 10 mA cm^{-2} at an overpotential of merely 81 mV, markedly lower than NF (362 mV), MoS_2 (290 mV), Ni_3Se_2 (210 mV), and even commercial Pt/C (120 mV). The overpotentials measured at 10, 50, and 100 mA cm^{-2} (Figure 5b) further underscore the exceptional catalytic performance of the heterostructures. The kinetic characteristics of the electrocatalytic process were further elucidated through Tafel analysis of the corresponding polarization curves (Figure 5c). MoS_2/Ni_3Se_2 heterostructure exhibits a markedly reduced Tafel slope of 31.75 mV dec^{-1}, significantly lower than those of NF (152.11 mV dec^{-1}), MoS_2 (124.98 mV dec^{-1}), Ni_3Se_2(95.74 mV dec^{-1}), and Pt/C (54.22 mV dec^{-1}), highlighting its enhanced reaction kinetics and revealing the hydrogen evolution reaction primarily follows a Volmer-Heyrovsky pathway [39]. The interfacial charge-transport characteristics were further investigated by electrochemical impedance spectroscopy (EIS), providing insight into the electron-transfer process at the electrode-electrolyte boundary. The Nyquist plots in Figure 5d reveal that MoS_2/Ni_3Se_2

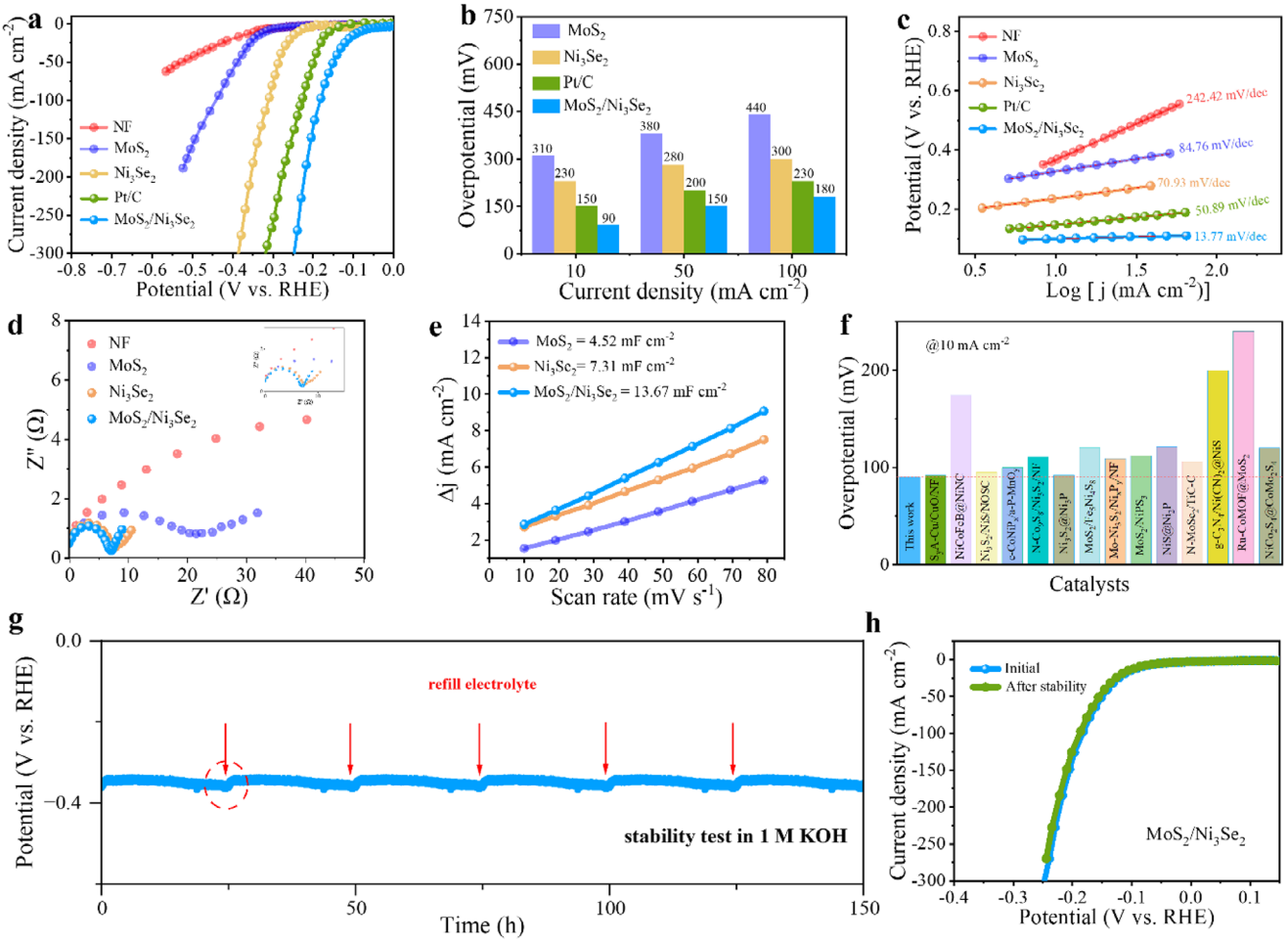

FIGURE 5 | Alkaline hydrogen evolution electrocatalysis: (a) LSV polarization curves; (b) Overpotentials at 10, 50, and 100 mA cm^{-2}; (c) Tafel slopes of NF, MoS_2, Ni_3Se_2, Pt/C, and MoS_2/Ni_3Se_2 heterostructures. (d) Electrochemical impedance plots (EIS); (e) C_{dl} values of MoS_2, Ni_3Se_2, and MoS_2/Ni_3Se_2, respectively. (f) Comparative assessment of the MoS_2/Ni_3Se_2 heterostructure and representative state-of-the-art electrocatalysts reported in the literature at 10 mA cm^{-2}. (g) Chronopotentiometric stability test at 10 mA cm^{-2}. (h) LSV polarization of MoS_2/Ni_3Se_2 before and after stability test.

possesses a markedly lower R_{ct} than NF, MoS_2, Ni_3Se_2, and Pt/C, evidencing accelerated charge transport at the heterointerface and more favorable reaction kinetics during electrocatalysis. This electrochemical behavior is fully consistent with the c-AFM observations, where the homogeneous current distribution and steeper local *I–V* characteristics demonstrate enhanced interfacial conductivity, thereby establishing a direct correlation between the microscopic charge-transport behavior and the reduced charge-transfer resistance responsible for the superior HER kinetics. To evaluate the density of accessible catalytic sites, the electrochemically active surface area (ECSA) was quantified using the double-layer capacitance (C_{dl}) obtained from cyclic voltammetry recorded in the non-Faradaic potential window (Figure S10). MoS_2/Ni_3Se_2 heterostructure displays a remarkable C_{dl} of 13.67 mF cm^{-2}, exceeding those of MoS_2 (4.52 mF cm^{-2}) and Ni_3Se_2 (7.31 mF cm^{-2}) (Figure 5e), suggesting a greater abundance of catalytically accessible active sites, which facilitate hydrogen adsorption and thereby enhance HER kinetics. It is pertinent to note that the rise in current density can be linked to either enhanced ECSA or intrinsic activity in the catalyst composition [40, 41]. It is important to look at the ECSA-normalized current density compared to the geometric-normalized density in the most catalytically active MoS_2/Ni_3Se_2 (Figure S11a). The comparative analysis of overpotential for the ECSA-normalized and geometric-normalized specific current density at (5 mA cm^{-2}) of MoS_2/Ni_3Se_2 (Figure S11b) shows significant enhancement in catalytic performance for the ECSA-normalized, suggesting that the intrinsic composition of the catalyst has a dominant role in the increase in surface area.

Moreover, the MoS_2/Ni_3Se_2 electrocatalyst exhibits outstanding activity and long-term stability, surpassing numerous recently reported non-noble-metal systems and positioning itself among the most efficient low-overpotential, high-stability catalysts (Figure 5f; Table S1). The durability of the heterostructure was further validated by long-term chronopotentiometry at 10 mA cm^{-2}, during which no appreciable increase in the operating potential was observed over 150 h of continuous electrolysis (Figure 5g). Such sustained activity reflects the exceptional structural integrity and chemical stability of the engineered heterointerface under extended operating conditions. The negligible deviation between the initial and post-stability polarization curves (Figure 5h) underscores the outstanding durability of the MoS_2/Ni_3Se_2 heterostructure, confirming its ability to maintain

catalytic performance during extended operation. Overall, the superior electrochemical behaviour of the MoS_2/Ni_3Se_2 heterostructure originates from accelerated charge-transfer kinetics, abundant accessible active sites, and strong interfacial electronic interactions that collectively facilitate the catalytic process. To enable direct comparison with the UOR measurements, the HER activity of the MoS_2/Ni_3Se_2 heterostructure was systematically assessed in 1 M KOH containing 0.5 M urea (Figure S12). The minimal effect of urea on intrinsic HER activity confirms the feasibility of coupling UOR and HER in a common alkaline urea electrolyte, thereby simplifying cell architecture and reducing fabrication costs for practical urea electrolysis systems.

2.4 | Urea Oxidation Electrocatalysis

As the anodic process governs water electrolysis and direct water splitting poses a significant challenge due to sluggish OER, the anodic OER was replaced with the UOR. The synthesized materials were tested as UOR anodes in a standard three-electrode setup at room temperature to probe their electrocatalytic performance. To elucidate the effect of urea concentration on reaction kinetics, the UOR activity of the MoS_2/Ni_3Se_2 heterostructure was examined in 1.0 M KOH over a range of urea concentrations, revealing its concentration-dependent catalytic behavior. Figure S13 demonstrates the strong urea oxidation capability of the MoS_2/Ni_3Se_2 heterostructure in an alkaline electrolyte. Increasing the urea concentration from 0.1 to 0.5 M promotes UOR, as evidenced by a substantial increase in anodic current density. Beyond this optimum concentration, the activity progressively decreases, likely owing to the excessive surface coverage of urea species that restricts OH^- adsorption at catalytic sites, thereby hindering C—N bond cleavage and slowing the overall reaction kinetics. These results demonstrate that electrolyte composition, particularly urea concentration, plays a critical role in governing the UOR performance by balancing urea availability and OH^- adsorption at the active interface. To distinguish the reaction kinetics of UOR from those of OER, LSV profiles were recorded in 1.0 M KOH with and without the addition of 0.5 M urea. As shown in Figure 6a, urea significantly enhances the anodic current density and shifts the polarization curve cathodically relative to OER. Notably, the current density of MoS_2/Ni_3Se_2 is 10 mA cm^{-2} at 1.20 V compared to 1.48 V for OER, suggesting faster kinetics and a lower energy barrier of UOR, which reduces the anodic potential and enhances energy efficiency. Figure 6b compares the UOR polarization behavior of MoS_2/Ni_3Se_2, MoS_2, Ni_3Se_2, bare NF, and the benchmark RuO_2 catalyst in 1.0 M KOH containing 0.5 M urea. The corresponding OER activity was evaluated in urea-free 1.0 M KOH, with the LSV curves shown in Figure S14. Remarkably, MoS_2/Ni_3Se_2 demonstrates the highest UOR performance, achieving the lowest onset potential of 1.20 V across all examined catalysts. Compared with pristine MoS_2, Ni_3Se_2, and RuO_2, the heterostructure attains 10, 50, and 100 mA cm^{-2} at markedly lower overpotentials, highlighting its enhanced electrocatalytic efficiency (Figure 6c). Tafel analysis (Figure 6d) indicates that the MoS_2/Ni_3Se_2 heterostructure displays a significantly reduced slope of 12.54 mV dec^{-1}, substantially lower than those of NF (98.73 mV dec^{-1}), MoS_2 (62.44 mV dec^{-1}), Ni_3Se_2 (56.81 mV dec^{-1}), and RuO_2 (19.54 mV dec^{-1}), reflecting markedly enhanced reaction energetics. The EIS results corroborate the superior charge-transfer kinetics of the heterostructure. As shown in Figure 6e, MoS_2/Ni_3Se_2 exhibits markedly lower charge-transfer resistance (R_{ct}), indicating enhanced electron transport at the electrode-electrolyte interface. As shown in Figure 6f and Table S2, the MoS_2/Ni_3Se_2 catalyst exhibits superior UOR activity compared with recently reported electrocatalysts. Recent advances in heterostructured and hierarchical electrode architectures have demonstrated enhanced electrocatalytic performance by regulating interfacial charge transport, optimizing active-site exposure, and improving operational stability under practically relevant current densities[42-45]. However, these strategies predominantly focus on activity enhancement through structural optimization, while the rational manipulation of interfacial electronic states remains insufficiently explored. In this work, the MoS_2/Ni_3Se_2 heterostructure introduces a work-function-driven built-in electric field that enables directional charge redistribution, which is systematically elucidated through combined UPS, XPS, DFT calculations, and operando structural investigations. This integrated approach establishes a direct correlation between interfacial electronic modulation and sustained catalytic activity with exceptional long-term durability. Beyond intrinsic catalytic activity, the long-term operational stability, an essential criterion for practical applications, was evaluated through chronopotentiometry measurements. Notably, the MoS_2/Ni_3Se_2 heterostructure delivers outstanding electrochemical robustness, sustaining stable operation with virtually no discernible loss in activity over 200 h at a current density of 10 mA cm^{-2} (Figure 6g). Inductively Coupled Plasma-Optical Emission Spectroscopy (ICP-OES) analysis of the sample drawn from the electrolyte after long-term durability test shows negligible elemental leaching (Table S3). The retention of virtually identical polarization behavior following long-term testing (Figure 6h) underscores the excellent electrochemical durability of the catalyst in 1 M KOH containing 0.5 M urea. To evaluate the structural resilience of the catalyst under UOR conditions, post-operando analyses were conducted following extended electrolysis. The recovered MoS_2/Ni_3Se_2 heterostructure was comprehensively characterized by XRD, XPS, SEM, and TEM (Figures S15–S17), providing insight into the preservation of its crystalline structure, surface chemistry, and morphology after prolonged operation.

The preserved crystallographic signatures in XRD confirm that the original MoS_2 and Ni_3Se_2 phases remain intact without detectable phase transformation during long-term UOR operation. Furthermore, the unchanged XPS chemical states indicate that the heterointerface effectively suppresses excessive surface oxidation and irreversible reconstruction under strongly alkaline and oxidative conditions. SEM and TEM analyses further reveal that the nanoscale morphology and intimate interfacial contact between MoS_2 and Ni_3Se_2 are maintained after 200 h of electrolysis, providing direct structural evidence for the mechanical robustness of the heterointerface. These observations demonstrate that the strong interfacial coupling between MoS_2 and Ni_3Se_2 prevents interfacial separation, structural collapse, and degradation of active sites during prolonged operation.

The preserved crystallographic signatures, invariant surface chemical states, and unchanged morphological features collectively demonstrate that the MoS_2/Ni_3Se_2 heterostructure maintains its structural coherence and interfacial integrity under extended electrochemical operation. The excellent agreement between the electrochemical durability and the post-operando

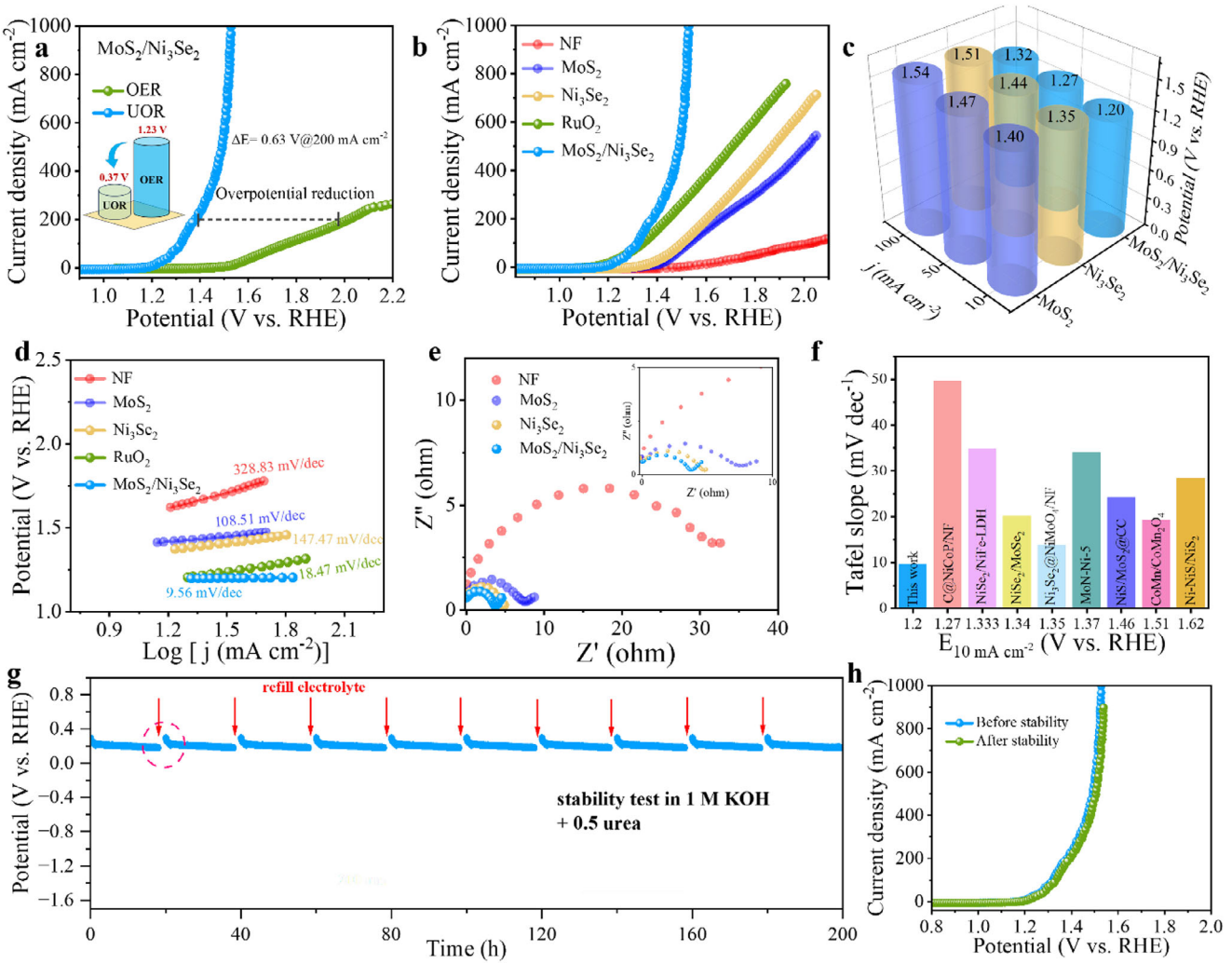

FIGURE 6 | Electrocatalytic activity and operational durability toward UOR. (a) Comparative OER and UOR LSV profiles of the MoS_2/Ni_3Se_2 electrocatalyst. (b) LSV profiles of UOR; (c) Potentials corresponding to benchmark current densities of 10, 50, and 100 mA cm^{-2}; (d) Tafel plots; and (e) Nyquist plots of the synthesized electrocatalysts. (f) Performance comparison of the MoS_2/Ni_3Se_2 heterostructure with representative advanced electrocatalysts previously reported for similar reactions. (g) Long-term chronopotentiometric stability measured at a constant current density of 10 mA cm^{-2}. (h) LSV profiles of MoS_2/Ni_3Se_2 before and after the stability test.

structural characterization confirms that the robust MoS_2/Ni_3Se_2 heterointerface effectively resists structural degradation and interfacial deterioration during prolonged UOR, thereby maintaining efficient charge transfer and sustained catalytic activity. These observations substantiate that the heterointerface, identified as the genuine catalytic locus, remains structurally and chemically stable throughout the reaction process.

On the basis of the above results, Scheme 1 depicts the proposed reaction mechanism for urea electrooxidation at the MoS_2/Ni_3Se_2 heterointerface. Charge transfer from Ni_3Se_2 to MoS_2 induces a built-in interfacial electric field, giving rise to electrophilic Ni_3Se_2 and nucleophilic MoS_2 domains. During UOR, urea is asymmetrically adsorbed at the MoS_2/Ni_3Se_2 interface, with its amino groups binding to electrophilic Ni_3Se_2 sites and its carbonyl moiety interacting with nucleophilic MoS_2 domains, driven by interfacial electrostatic forces. Such heterointerface-driven electronic regulation enhances the activation of urea molecules and weakens the C—N bond, thereby promoting the reaction kinetics of urea electrooxidation.

2.5 | In Situ Electrochemical Raman Spectroscopy

In situ electrochemical Raman spectroscopy was employed to monitor the real-time compositional evolution of the catalyst under operating conditions, thereby elucidating the electrochemical pathways and catalytic mechanisms of the UOR and OER. Figure 7a–c presents the in situ Raman spectra of the MoS_2/Ni_3Se_2 heterostructure collected in 1 M KOH containing 0.5 M urea over an applied potential window of 1.20–1.60 V vs. RHE. During UOR catalysis, two broad vibrational bands emerge in the 400–580 cm^{-1} region at potentials below 1.40 V. Upon increasing the applied potential beyond 1.35 V, these initially broad features evolve into well-defined doublet peaks centered at 453 and 565 cm^{-1}. These bands are assigned to the Ni-O bending and

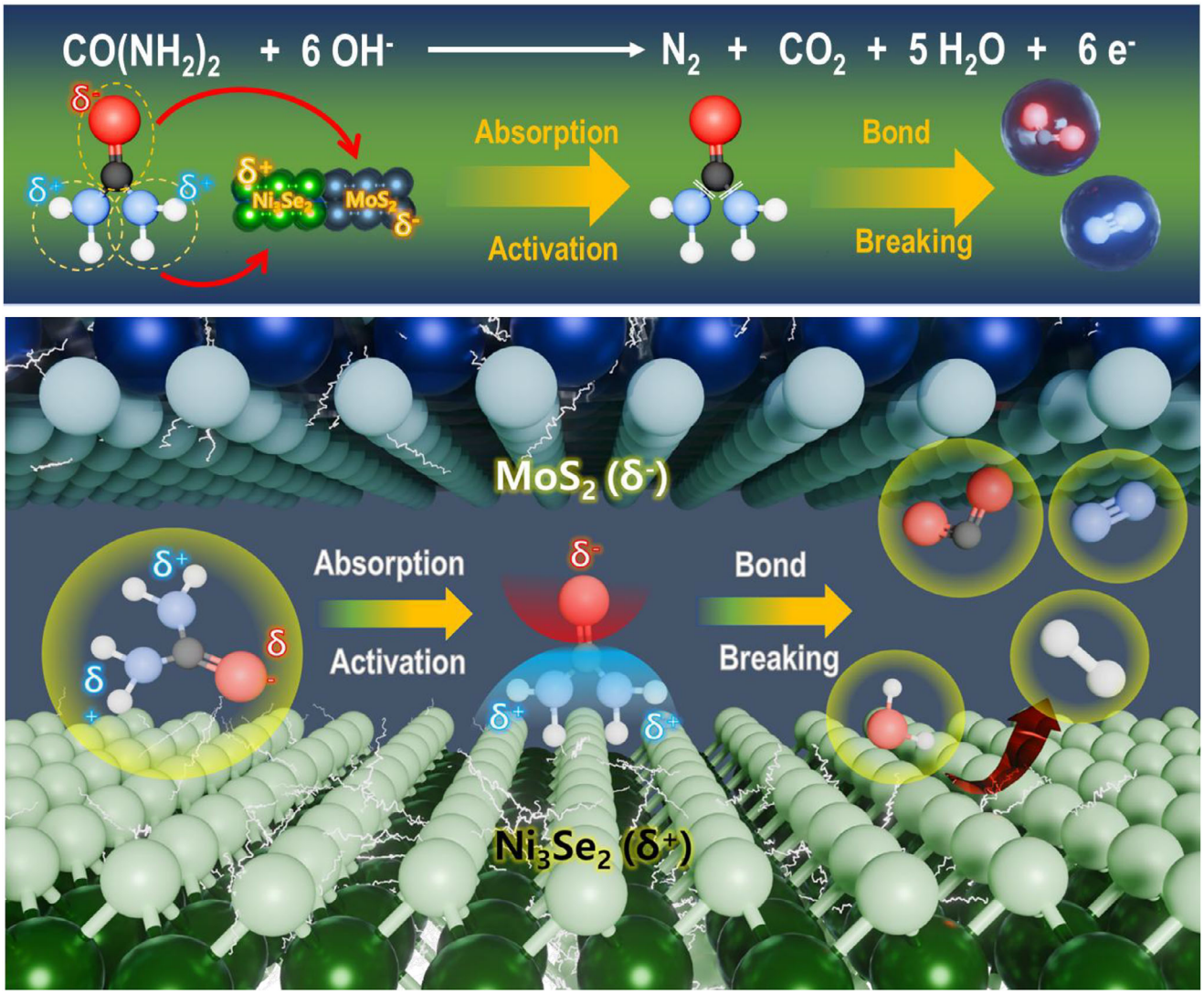

SCHEME 1 | Illustration of the heterointerface-regulated UOR process on MoS_2/Ni_3Se_2, showing the synergistic electronic interactions that govern intermediate adsorption and reaction kinetics.

stretching modes, respectively, signifying the electrochemical transformation of $Ni(OH)_2$ to NiOOH. Concurrently, a distinct band centered at ~1000 cm^{-1}, attributed to the C—N stretching vibration of urea, progressively decreases in intensity with increasing potential, indicating potential-driven oxidation of the amide bond within the urea molecule. The in situ generation of NiOOH, together with the pronounced suppression of the C–N stretching vibration, provides direct evidence for the anodic oxidation of Ni species (Equation 1) and the subsequent NiOOH-mediated oxidation of urea, ultimately resulting in cleavage of the C—N bond (Equation 2). The simultaneous evolution of the NiOOH and C—N Raman bands indicates that the electrochemically generated NiOOH is continuously involved in urea oxidation rather than undergoing excessive accumulation on the catalyst surface, thereby supporting the preferential UOR pathway under operating conditions.

$$6Ni(OH)_2\,(s) + 6OH^- \leftrightarrow 6NiOOH\ (s) + 6H_2O\,(l) + 6e^- \quad (1)$$

$$CO(NH_2)_2\ (aq) + 6NiOOH\ (s) + H_2O\ (l) \rightarrow N_2\ (g) + CO_2\ (g) + 6Ni(OH)_2\ (s) \quad (2)$$

During OER conditions (Figure 7d–f), the characteristic C—N stretching vibration is absent, while the Ni—O Raman feature becomes discernible only at an applied potential of 1.45 V. This delayed emergence indicates that NiOOH formation occurs at higher potentials in the absence of urea, confirming that urea oxidation is initiated at significantly lower potentials and exhibits more favorable kinetics than the OER under identical conditions.

To elucidate the influence of the heterostructure on urea adsorption behavior, open-circuit potential (OCP) and temperature-programmed desorption (TPD) measurements were conducted on MoS_2, Ni_3Se_2, and the MoS_2/Ni_3Se_2 heterostructure [37, 46]. The exchange of OH^- ion in the Helmholtz layer occurs at the surface of the electrode following the adsorption of organic molecules, which leads to a decrease in OCP. The OCP measurement for MoS_2/Ni_3Se_2, Ni_3Se_2, and MoS_2 was carried out to verify the adsorption behavior of urea on the electrocatalyst (Figure 7g). The OCP of the catalyst was tested in 1 M KOH for 100 s, followed by the injection of 0.5 M urea and another 100 s of testing. The hybrid MoS_2/Ni_3Se_2 shows a larger OCP reduction (0.268 V) compared to Ni_3Se_2 (0.241 V) and MoS_2 (0.163 V), which

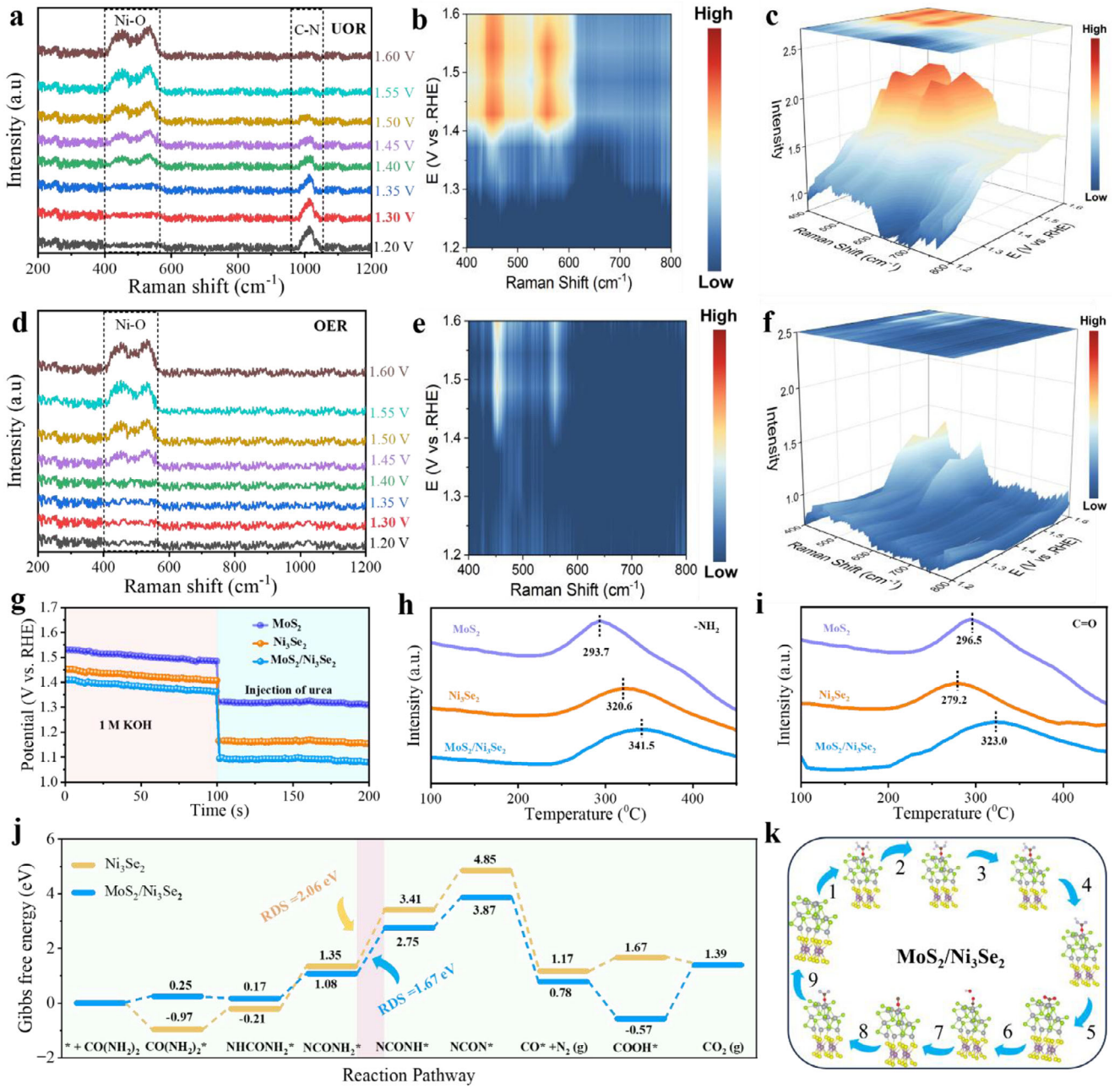

FIGURE 7 | Mechanistic investigation of the electrocatalytic process. In situ Raman spectra and corresponding contour maps, together with in situ FTIR spectra of adsorbed urea species on the MoS_2/Ni_3Se_2 heterostructure, were recorded under applied potentials during the urea oxidation reaction (a–c) and oxygen evolution reaction (d–f), revealing the evolution of reaction intermediates and potential-dependent surface reconstruction. (g) OCP measurements of MoS_2, Ni_3Se_2, and MoS_2/Ni_3Se_2 were measured in 1.0 M KOH electrolyte, followed by the injection of 0.5 M urea into the electrolyte at 100 s. TPD adsorption profiles of MoS_2, Ni_3Se_2, and MoS_2/Ni_3Se_2 heterostructures measured under (h) butylamine/He and (i) CO atmospheres. (j) Theoretical free-energy profiles of Ni_3Se_2 and MoS_2/Ni_3Se_2 heterostructure. (k) Reaction intermediates and corresponding elementary steps along the UOR pathway on MoS_2/Ni_3Se_2. Gray, purple, yellow, light green, red, dark brown, light blue, and light pink spheres represent Ni, Mo, S, Se, O, C, N, and H atoms, respectively.

suggests enhanced urea adsorption capacity in the heterostructure. Furthermore, the adsorption properties of functional groups on MoS_2/Ni_3Se_2, Ni_3Se_2, and MoS_2 were studied via TPD testing (Figure 7h,i). The urea molecule comprises two characteristic functional groups, namely a carbonyl group (C═O bond) and a pair of amino groups (—NH_2). The preferred adsorption sites (Ni or Mo) on MoS_2/Ni_3Se_2 were revealed by carrying out the TPD experiments in CO and NH_3 atmospheres, respectively. In the presence of a butylamine/He atmosphere, Ni_3Se_2 exhibits a higher desorption temperature of 320.6°C compared to MoS_2 (293.7°C), indicating that Ni_3Se_2 possesses stronger adsorption behavior toward the —NH_2 group. On the other hand, MoS_2 exhibits a higher desorption temperature (296.5°C) in the presence of CO compared to Ni_3Se_2 (279.2°C), suggesting a stronger adsorption capacity of MoS_2 toward C═O. The desorption temperature of the heterostructure MoS_2/Ni_3Se_2 is unexpectedly higher

than the individual components, both in the presence of —NH_2 and C═O, which could be attributed to synergistic enhancement of adsorption capacity by the heterojunction interface.

2.6 | DFT Calculations

The enhanced UOR and HER activities of the MoS_2/Ni_3Se_2 heterostructure were elucidated by DFT calculations, which reveal strong interfacial coupling accompanied by pronounced charge redistribution and electronic interactions governing the reaction mechanisms. These DFT results provide atomistic mechanistic interpretations that complement the experimentally observed electrocatalytic performance and are discussed separately from the experimental observations. For comparison, theoretical models of pristine MoS_2 and Ni_3Se_2 were constructed based on the HRTEM and XRD data, and the optimized atomic structure of the MoS_2/Ni_3Se_2 heterostructure is shown in Figure 8a. The DFT model was established using the experimentally observed $MoS_2(100)/Ni_3Se_2(110)$ interface to represent the synthesized heterostructure. Since the built-in electric field originates from the intrinsic work-function mismatch between MoS_2 and Ni_3Se_2, alternative interface orientations are expected to cause only minor variations in the calculated energetics without changing the overall trends in charge transfer and catalytic activity. The adsorption energetics of urea and OH* at the MoS_2/Ni_3Se_2 heterointerface were first systematically assessed (Figure 8b). As shown in Figure 8b, the substantially lower adsorption energy of urea (−1.85 eV) compared to OH^- (2.71 eV) reveals a pronounced preferential surface affinity for urea, thereby favoring kinetically accelerated UOR over the competing OER, in excellent consistency with the electrochemical results. To clarify how interfacial adsorption governs catalytic reactivity, the adsorption energies associated with the carbonyl (C═O) and amino (—NH_2) groups of urea were calculated on MoS_2 and Ni_3Se_2, respectively (Figure S18). The results reveal a complementary adsorption preference: Ni_3Se_2 favors —NH_2 binding, whereas MoS_2 exhibits a stronger affinity for the C═O group, highlighting synergistic interfacial effects relevant to urea activation. In addition, as illustrated in Figure S19, the MoS_2/Ni_3Se_2 heterostructure exhibits a substantially more negative urea adsorption energy (−1.85 eV) than pristine MoS_2 (−0.99 eV) or Ni_3Se_2 (−1.12 eV), indicating that heterointerface construction synergistically integrates and amplifies the intrinsic advantages of the individual components, thereby optimizing urea adsorption.

For alkaline HER, the rate-determining steps involve water dissociation and subsequent hydrogen adsorption on the catalyst surface. Guided by Sabatier's principle, an ideal hydrogen-evolution catalyst features a near-thermoneutral Gibbs free energy of hydrogen adsorption (ΔG_{H^*}), motivating the calculation of ΔG_{H^*} for the catalyst to assess its H* binding characteristics. Figure 8c depicts the Gibbs free-energy profiles for H* adsorption on MoS_2, Ni_3Se_2, and MoS_2/Ni_3Se_2 catalysts. For MoS_2/Ni_3Se_2, DFT calculations reveal site-dependent hydrogen adsorption, with ΔG_{H^*} values of −0.11 eV at the Ni site and −0.08 eV at the Mo site, highlighting near-thermoneutral H* binding at the Mo site. This is expected since the MoS_2 component of the heterostructure is negatively charged while the Ni_3Se_2 component is positively charged, creating a highly polarized interface that facilitates the capacity of H^+ to selectively adsorb on the Mo site. By contrast, pristine MoS_2 and Ni_3Se_2 display appreciably positive hydrogen adsorption free energies (ΔG_{H^*} = 0.35 and 0.15 eV, respectively), indicative of intrinsically weak binding of the H* intermediate. In MoS_2, the Mo sites serve as the primary HER active centers, whereas in the MoS_2/Ni_3Se_2 heterostructure, the Mo and Ni sites become the dominant catalytic sites due to the built-in electric field at the heterostructure, which drives electron transfer from Ni_3Se_2 to MoS_2 and induces interfacial electron redistribution. Consequently, the ΔG_{H^*} at the Mo site in MoS_2/Ni_3Se_2 approaches thermoneutrality, establishing an ideal balance between hydrogen adsorption and desorption [47, 48].

To elucidate the origin of the enhanced conductivity, we performed partial density of states (PDOS) (Figure 8d–f). PDOS confirms that MoS_2 preserves its characteristic semiconducting behavior, exhibiting a bandgap of ∼2.01 eV. By contrast, Ni_3Se_2 exhibits a substantial electronic-state accumulation in the vicinity of the Fermi level, indicative of enhanced charge-carrier transport and more efficient interfacial electron-transfer processes. Compared with single-phase MoS_2 and Ni_3Se_2, the MoS_2/Ni_3Se_2 heterostructure exhibits a higher electronic-state density near the Fermi level, thereby facilitating superior conductivity and accelerated charge-transfer kinetics [49]. This facilitates robust electronic coupling between the adsorbed reaction intermediates and the MoS_2/Ni_3Se_2 surface throughout the HER and UOR processes. The d-band center (E_d) is widely recognized as an effective descriptor of the adsorbate-catalyst interaction. As shown in Figure S20, the calculated E_d values for MoS_2/Ni_3Se_2, MoS_2, and Ni_3Se_2 are −1.20, −1.32, and −1.19 eV, respectively, with an intermediate E_d for MoS_2/Ni_3Se_2 that enables an optimal balance between adsorption and desorption of reaction intermediates, thereby underpinning its enhanced HER and UOR performance.

The efficiency of interfacial charge transfer is fundamentally dictated by the electronic propensity of charge carriers to migrate across the interface, a characteristic that is quantitatively reflected by the work function ($\boldsymbol{\Phi}$) [50]. The calculated work functions of MoS_2 and Ni_3Se_2 are 5.41 and 5.12 eV, respectively, facilitating spontaneous electron transfer across the MoS_2/Ni_3Se_2 interface (Figure 8g,h). Owing to the mismatch in work functions, electrons spontaneously transfer from Ni_3Se_2 to MoS_2, resulting in interfacial charge redistribution and the establishment of a built-in electric field until the Fermi levels of the two components become aligned (Figure 8i) [34]. This interfacial charge transfer induces electron depletion in Ni_3Se_2 while simultaneously enriching MoS_2 with electrons, rendering the latter electron-rich. The resulting interfacial band alignment, together with the built-in electric field at the MoS_2/Ni_3Se_2 junction, drives pronounced charge redistribution. Consequently, the electron-rich MoS_2 surface provides energetically favorable sites for the adsorption and activation of urea-derived intermediates, thereby significantly enhancing the catalytic performance.

Furthermore, the differential charge density analysis clearly demonstrates substantial charge redistribution at the interface, with electrons preferentially flowing from Ni_3Se_2 toward MoS_2, resulting in electron depletion within Ni_3Se_2 and concomitant accumulation on MoS_2 (Figure 8j). Quantitative Bader charge analysis confirms a net transfer of ∼2.34 e across the MoS_2/Ni_3Se_2 interface, evidencing strong electronic interaction and intimate interfacial coupling between the two components. To elucidate

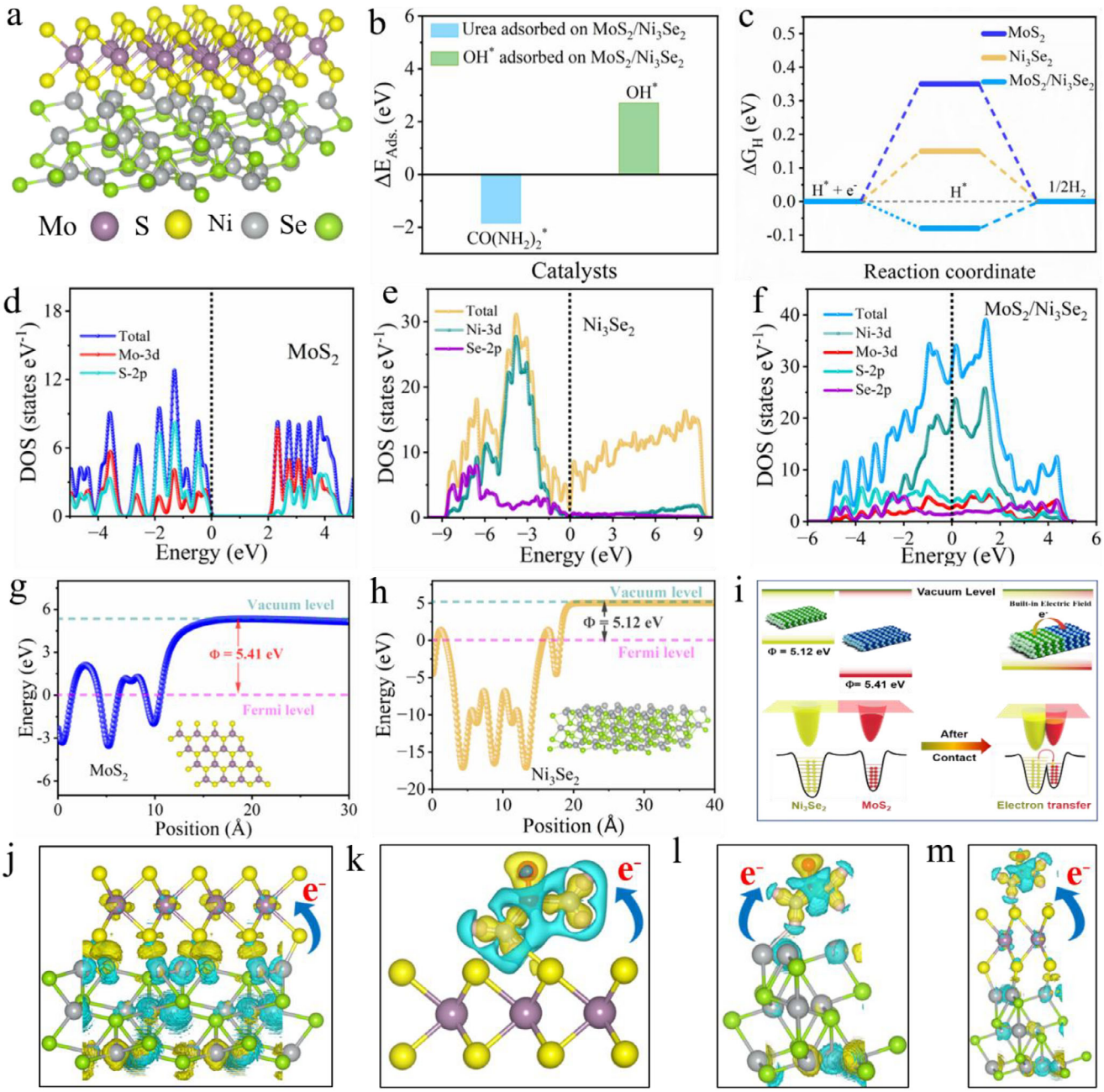

FIGURE 8 | DFT elucidation of the MoS_2/Ni_3Se_2 heterostructure. (a) Optimized Structural models of the MoS_2/Ni_3Se_2 heterostructure. (b) Relative adsorption energies of urea and OH^- on MoS_2/Ni_3Se_2 heterostructure. (c) The Gibbs free energies of adsorption for the MoS_2/Ni_3Se_2 heterostructure and its constituent components. PDOS of (d) MoS_2, (e) Ni_3Se_2, and (f) MoS_2/Ni_3Se_2 heterostructure. Calculated work functions of (g) MoS_2 and (h) Ni_3Se_2. Schematic band structures of MoS_2 and Ni_3Se_2 (i) before and after the formation of the interface. (j) Differential charge density of MoS_2/Ni_3Se_2 heterostructure at equilibrium, with yellow and cyan isosurfaces (1.21×10^{-3} e bohr^{-3}) indicating electron accumulation and depletion, respectively. Charge redistribution and Bader charge analysis of urea adsorption on the surface of (k) MoS_2, (l) Ni_3Se_2, and (m) MoS_2/Ni_3Se_2 heterostructure.

the correlation between functional-group adsorption and catalytic performance, charge-density-difference and Bader charge analyses were carried out on urea adsorption on MoS_2, Ni_3Se_2, and the MoS_2/Ni_3Se_2 heterostructure (Figure 8k–m). Bader analysis reveals that urea gains a significantly higher negative charge on MoS_2/Ni_3Se_2 (−1.25 e) compared with pristine Ni_3Se_2 (−0.98 e) and MoS_2 (−0.36 e), indicating that the heterostructure enriches electron density on the adsorbed intermediate, thereby strengthening urea binding and reducing the UOR overpotential.

The strong electronic coupling at the MoS_2/Ni_3Se_2 interface facilitates the tailored adsorption and desorption of reaction intermediates, offering an effective strategy to enhance the stepwise UOR kinetics. Next, the Gibbs free energy changes (ΔG) were computed to elucidate the mechanistic pathway of the UOR. Figure 7j presents the ΔG profiles for each UOR step on MoS_2/Ni_3Se_2 and Ni_3Se_2, revealing that the rate-determining step (RDS) for both catalysts is the third dehydrogenation step ($CO(NH_2{\cdot}N)^* \rightarrow CO(NH{\cdot}N)^*$). Importantly, the formation of the

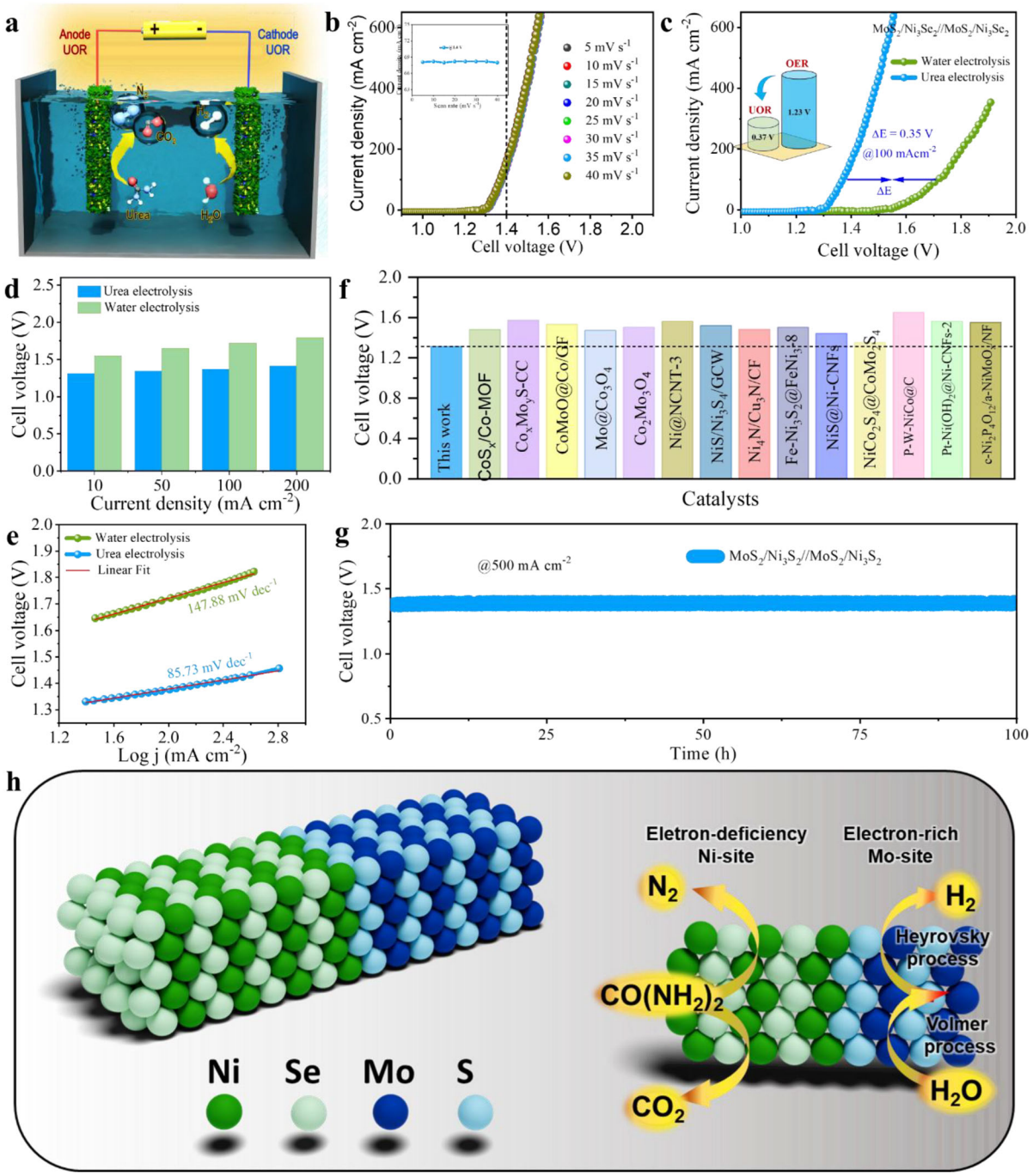

FIGURE 9 | Electrocatalytic performance of urea and water electrolysis. (a) Schematic illustration depicting the complete urea electrolysis process. (b) LSV profiles of MoS_2/Ni_3Se_2 at varying scan rates (inset: current densities at 1.40 V). (c) LSV comparison of MoS_2/Ni_3Se_2 in 1.0 M KOH with and without 0.5 M urea. (d) Cell voltage required to deliver current densities of 10, 50, 100, 200 mA cm^{-2}; (e) Corresponding Tafel slopes of the UOR//HER system under both conditions. (f) Cell voltages at 10 mA cm^{-2} for MoS_2/Ni_3Se_2 as both anode and cathode in contrast to earlier transition-metal-based bifunctional electrocatalysts reported in the literature. (g) Stability of MoS_2/Ni_3Se_2 under dual-electrode configuration. (h) Schematic of the HER and UOR mechanisms on MoS_2/Ni_3Se_2.

MoS_2/Ni_3Se_2 heterostructure markedly reduces the thermodynamic barrier to 1.67 eV, in sharp contrast to the substantially higher value of 2.06 eV for pristine Ni_3Se_2, underscoring the heterointerface-driven lowering of the reaction energy barrier. On MoS_2/Ni_3Se_2, the RDS at the Ni sites displays a markedly reduced energy barrier compared to the single-phase electrocatalyst, suggesting that the abundant MoS_2/Ni_3Se_2 interfaces facilitate the adsorption–desorption dynamics of key intermediates during the UOR process (Figure 7k). Collectively, these DFT results provide a mechanistic interpretation of the experimentally observed enhanced electrocatalytic activity of the MoS_2/Ni_3Se_2 system by elucidating the roles of interfacial charge redistribution, optimized adsorption energetics, and reduced reaction-energy barriers.

2.7 | Overall Urea Electrolysis Performance

Motivated by the excellent HER and UOR activities of the MoS_2/Ni_3Se_2 heterostructure, a two-electrode electrolyzer was constructed to assess its overall urea electrolysis performance, using MoS_2/Ni_3Se_2 as a bifunctional catalyst in 1 M KOH containing 0.5 M urea (Figure 9a). LSV measurements were conducted over a range of scan rates (5–40 mV s^{-1}) to investigate the electrochemical behavior of the MoS_2/Ni_3Se_2 heterostructure under the specified conditions (Figure 9b). The UOR performance shows no significant dependence on scan rate over the full range of applied current densities, suggesting highly efficient interfacial charge-transfer kinetics and minimal contribution from capacitive processes during bifunctional operation. For comparison, the performance of overall water splitting was tested under identical conditions in 1 M KOH (Figure S21). As illustrated in Figure 9c, the urea-assisted electrolyzer delivers a current density of 10 mA cm^{-2} at a remarkably low cell voltage of 1.31 V, which is significantly lower than the 1.55 V required for conventional water electrolysis under identical conditions. This pronounced decrease demonstrates that replacing the anodic OER with urea oxidation substantially reduces the thermodynamic energy barrier, thereby enabling a more energy-efficient pathway for HER. Moreover, the $MoS_2/Ni_3Se_2//MoS_2/Ni_3Se_2$ electrolyzer delivers current densities of 50, 100, and 200 mA cm^{-2} at exceptionally low cell voltages of 1.34, 1.37, and 1.41 V, respectively, which are markedly lower than the corresponding voltages of 1.65, 1.72, and 1.79 V required for OER-driven operation (Figure 9d). Tafel slope analysis reveals distinctly different reaction kinetics between the two configurations. The HER//OER system shows a significantly larger slope of 147.88 mV dec^{-1} compared to 85.73 mV dec^{-1} for the HER//UOR system (Figure 9e), indicating slower charge-transfer kinetics in the former. Remarkably, the MoS_2/Ni_3Se_2 device delivers urea electrolysis at an ultralow cell voltage while maintaining a stable current density of 10 mA cm^{-2}, thereby ranking among the most energy-efficient systems reported to date (Figure 9f). Finally, the MoS_2/Ni_3Se_2 catalyst demonstrates outstanding stability under UOR//HER operation, sustaining a constant potential with negligible current decay during continuous electrolysis at 500 mA cm^{-2} for 100 h (Figure 9g). The generated gases during urea electrolysis were collected and analyzed using a gas chromatograph at 20 min intervals. This analysis revealed that only hydrogen and nitrogen were produced (Figure S22). The amount of gases was found to have linearly increased over time, with a hydrogen production rate of 8.28.7 μmol/hr and an N_2 production rate of 6.89 μmol/hr. The average Faradaic efficiency for H_2 and N_2 production was found to be 97.8% and 91.98%, respectively.

The intrinsic factors responsible for the superior HER and UOR performance of MoS_2/Ni_3Se_2 are schematically illustrated in Figure 9h. In the MoS_2/Ni_3Se_2 heterostructure, electron-deficient Ni sites exhibit enhanced *d-p* hybridization coupling with the O 2p states of urea, with Ni 3d states positioned below the Fermi level, identifying these sites as the primary active centers for UOR. In contrast, the Mo 3d orbitals show higher electron occupation and preferential hybridization with H 1s states, rendering Mo sites predominantly active for the HER. Furthermore, in the MoS_2/Ni_3Se_2 heterostructure, water dissociation preferentially occurs at the Mo sites, where the resulting H* intermediates are stabilized through Mo-H bonding and receive electrons from the Mo centers. Thus, the presence of dual catalytically active sites, together with their synergistic interplay arising from an optimized d-band center and strong d-d electronic coupling, endows the system with exceptional UOR and HER performance.

3 | Conclusion

In summary, a MoS_2/Ni_3Se_2 heterostructure electrocatalyst featuring an intrinsic built-in electric field was rationally constructed via a combined hydrothermal and electrodeposition strategy. The intimate MoS_2/Ni_3Se_2 interface induces a strong built-in electric field arising from interfacial band alignment, which modulates the surface electronic structure. This configuration facilitates interfacial charge transfer, increases accessible surface area, and enhances the density of electrochemically active sites, thereby accelerating reaction kinetics. As a result, the catalyst delivers a current density of 10 mA cm^{-2} at low overpotentials of 81 mV for the HER and 1.20 V for UOR in 1.0 M KOH containing 0.5 M urea. DFT calculations indicate that asymmetric interfacial charge redistribution tunes the hydrogen adsorption free energy toward thermoneutrality ($\Delta G_{H^*} \approx 0$), thereby promoting HER activity, while simultaneously lowering the energy barrier of the rate-determining step in UOR. Furthermore, a two-electrode electrolyzer employing MoS_2/Ni_3Se_2 as both cathode and anode achieves a cell voltage of 1.31 V at 10 mA cm^{-2}, comparable to or better than many reported transition-metal-based bifunctional electrocatalysts. Overall, this work highlights built-in electric-field-driven heterostructure engineering as an effective strategy for designing efficient bifunctional electrocatalysts for sustainable hydrogen production.

Author Contributions

Boka Fikadu Banti: conceptualization, investigation, writing – original draft, writing – review and editing, visualization, validation, methodology, software, formal analysis, data curation. **Hyojin Kang**: conceptualization, validation, formal analysis, writing – review and editing. **Indra Memdi Khoris**: conceptualization, investigation, formal analysis, data curation. **Cheru Fekadu Molla**: conceptualization, investigation, funding acquisition, writing – original draft, writing – review and editing, visualization, validation, methodology, formal analysis, project administration, supervision. **Birhanu Bayissa Gicha**: writing – review and editing, data curation, methodology. **Jihyeon Yeom**: conceptualization, investigation, data curation, writing – review and editing. **Njemuwa Nwaji**: conceptualization, investigation, writing – original draft, writing – review and editing, validation, methodology, formal analysis, supervision, data curation. **Jaebeom Lee**: conceptualization, investigation, funding acquisition, writing – original draft, writing – review and editing, visualization, validation, methodology, formal analysis, project administration, supervision.

Acknowledgements

This work was supported by the National Research Foundation of Korea (NRF) grant funded by the Korean government (MSIT) number RS-2024-00333541. This research was also supported by the Nano & Material Technology Development Program through the (RS-2026-25604779)

Conflicts of Interest

J.L. is the founder of SpinPlas Solution Inc. The company may have a potential financial interest in the subject matter of this article.

Data Availability Statement

The data that support the findings of this study are available from the corresponding author upon reasonable request.

References

1. C. Xuan, Q. Xu, L. Han, and B. Hou, "Electronic Structure Exquisite Modulation of $NiSe_2$ Interface via Rationally Controlling Fe Doping for Boosting Electrochemical Oxygen Evolution Activity," *Chemical Engineering Journal* 464 (2023): 142620, https://doi.org/10.1016/j.cej.2023.142620.

2. Z. Ma, X. Liu, H. Wang, et al., "Interfacial Engineering of NiCo Nanocones to Promote NiOOH Formation via Enhanced Dehydrogenation for Efficient Urea Electrooxidation," *Advanced Energy Materials* 16 (2026): 02563, https://doi.org/10.1002/aenm.202502563.

3. C. Yang, H. Pang, X. Li, et al., "Scalable Electrocatalytic Urea Wastewater Treatment Coupled With Hydrogen Production by Regulating Adsorption Behavior of Urea Molecule," *Nano-Micro Letters* 17 (2025): 159, https://doi.org/10.1007/s40820-024-01585-0.

4. C. R. Deng, H. Yao, Y. Wang, et al., "Interface Effect of Fe Doped NiSe/Ni_3Se2 Heterojunction as Highly Efficient Electrocatalysts for Overall Water Splitting," *Chemical Engineering Journal* 488 (2024): 150996, https://doi.org/10.1016/j.cej.2024.150996.

5. J.-W. Zhao, K. Yue, H. Zhang, et al., "The Formation of Unsaturated IrOx in SrIrO3 by Cobalt-doping for Acidic Oxygen Evolution Reaction," *Nature Communications* 15 (2024): 2928, https://doi.org/10.1038/s41467-024-46801-y.

6. W. Jiang, J. Zhang, J. Wu, et al., "Regulating the Competitive Adsorption of Urea and OH− via Brønsted Base Intercalated Nickel Sites for Highly Selective Urea Oxidation," *Advanced Energy Materials* 16 (2026): 03978, https://doi.org/10.1002/aenm.202503978.

7. B. F. Banti, H. Kang, S. Asgaran, et al., "Ni (CN)2@ NiS Anchored on Graphitic Carbon Nitride as an Advanced Functional Electrode for Self-powered Hydrazine-assisted Hydrogen Generation," *International Journal of Hydrogen Energy* 200 (2026): 152831, https://doi.org/10.1016/j.ijhydene.2025.152831.

8. H. Qin, J. Li, G. Lin, et al., "Tuning Surface Coordination Environment of Ni3N by Fluorine Modification for Efficient Methanol Electrooxidation Assisted Hydrogen Evolution," *Advanced Materials* 37 (2025): 2507573, https://doi.org/10.1002/adma.202507573.

9. Z. Zhao, H. Zeng, Y. Zhou, M. Yuan, and X. Chang, "Synergistic Catalytic Mechanism of Cyanide-bridged Ni-Fe Bimetallic Electrocatalyst for Highly Efficient Urea Oxidation," *Applied Catalysis B: Environment and Energy* 375 (2025): 125414, https://doi.org/10.1016/j.apcatb.2025.125414.

10. H. M. Xu, K. H. Yue, L. J. Song, et al., "The Asymmetrical Fe−O−Se Bonds in Fe_2 $O(SeO_3)_2$ Boosting Bifunctional Oxygen Electrocatalytic Performance for Zinc-Air Battery," *Angewandte Chemie International Edition* 63 (2024): 202412025, https://doi.org/10.1002/anie.202412025.

11. B. F. Banti, B. B. Gicha, M. Goddati, et al., "Molecular-Level Engineered Approach Induces Built-in Electric Field Modulation in G-$C3N_4$/$CoMoS_2$ Heterojunction for Enhanced Hydrogen Generation via Urea Oxidation," *Small* 22 (2026): e73842.

12. L. Wang, Y. Zhu, Y. Wen, et al., "Regulating the Local Charge Distribution of Ni Active Sites for the Urea Oxidation Reaction," *Angewandte Chemie International Edition* 60 (2021): 10577–10582.

13. X. Zhu, M. Ge, X. Yuan, Y. Wang, and Y. Tang, "Unveiling the Mechanistic Landscape and Advantages of Two-dimensional Phthalocyanine in Sustainable Urea Synthesis," *Applied Catalysis B: Environment and Energy* 363 (2025): 124826, https://doi.org/10.1016/j.apcatb.2024.124826.

14. Y. Zhang, X. Zhen, Z. Su, J. Guo, J. Li, and X. Li, "Ni/MoC@ NC as Bifunctional Electrocatalyst Coupled HER and Urea Oxidation for Energy-efficient Hydrogen Production," *International Journal of Hydrogen Energy* 60 (2024): 46–54, https://doi.org/10.1016/j.ijhydene.2024.02.106.

15. F. Yang, S. Lu, Y. Feng, L. Fu, and L. Feng, "Insights Into the Confinement Effect of NiMo Catalysts Toward Alkaline Hydrogen Oxidation," *ACS Catalysis* 14 (2024): 2324–2332, https://doi.org/10.1021/acscatal.3c06058.

16. Y. Li, X. Yu, Y. Fan, et al., "Electrochemical Exfoliation of the Two-Dimensional Conjugated Metal–Organic Framework for High-Performance Urea Electrooxidation," *ACS nano* 19 (2025): 18781–18790, https://doi.org/10.1021/acsnano.5c04006.

17. X. Xu, C. Zhang, J. Li, et al., "Redistributing Interfacial Charge Density of Ni12P5/Ni3P via Fe Doping for Ultrafast Urea Oxidation Catalysis at Large Current Densities," *Chemical Engineering Journal* 452 (2023): 139362, https://doi.org/10.1016/j.cej.2022.139362.

18. G. Huang, Y. Huang, A. Ali, et al., "Phase-Controllable Cobalt Phosphide Heterostructure For Efficient Electrocatalytic Hydrogen Evolution In Water And Seawater," *Electron* 2 (2024): 58, https://doi.org/10.1002/elt2.58.

19. X. Chu, C. Sathish, J. H. Yang, et al., "Sodium Chloride-Assisted Crystalline Graphitic Carbon Nitride for Efficient Photocatalytic Hydrogen Evolution," *Electron* 3 (2025): 70000, https://doi.org/10.1002/elt2.70000.

20. Y. Pan, J. Gao, and I. Jain, "Revealing the Structural, Catalytic Properties and Dehydrogenated Behavior of Nb2C MXene for Hydrogen Evolution Reaction (HER)," *Material Today Energy* (2025): 102022.

21. M. Pan, G. Qian, T. Yu, et al., "Ni Modified Co2VO4 Heterojunction With Poor/Rich-electron Structure for Overall Urea-rich Wastewater Oxidation," *Chemical Engineering Journal* 435 (2022): 134986, https://doi.org/10.1016/j.cej.2022.134986.

22. X. Xu, H. Liao, L. Huang, et al., "Surface Reconstruction and Directed Electron Transport in $NiSe_2$/$MoSe_2$ Mott-Schottky Heterojunction Catalysts Promote Urea-assisted Water Splitting," *Applied Catalysis B: Environmental* 341 (2024): 123312, https://doi.org/10.1016/j.apcatb.2023.123312.

23. K. Wang, W. Huang, Q. Cao, et al., "Engineering NiF_3/Ni2P Heterojunction as Efficient Electrocatalysts for Urea Oxidation and Splitting," *Chemical Engineering Journal* 427 (2022): 130865, https://doi.org/10.1016/j.cej.2021.130865.

24. C. Liu, X. Cao, L. Chen, et al., "Synergistic Urea Oxidation and Hydrogen Evolution Over MoC/Co/NCNT-based Electrocatalysts for Cost-effective Alkaline Electrolysis," *ACS Catalysis* 15 (2025): 14983–14995, https://doi.org/10.1021/acscatal.5c03492.

25. M. Du, Y. Ji, Y. Li, S. Liu, and J. Yan, "Construction of an Internal Charge Field: CoS1. 097/Ni_3S_2 Heterojunction Promotes Efficient Urea Oxidation Reaction," *Advanced Functional Materials* 34 (2024): 2402776, https://doi.org/10.1002/adfm.202402776.

26. T. Wang, L. Miao, S. Zheng, et al., "Interfacial Engineering of Ni3N/Mo2N Heterojunctions for Urea-assisted Hydrogen Evolution Reaction," *American Chemical Society Catalysis* 13 (2023): 4091–4100.

27. Q. Qian, J. Zhang, J. Li, et al., "Artificial Heterointerfaces Achieve Delicate Reaction Kinetics towards Hydrogen Evolution and Hydrazine Oxidation Catalysis," *Angewandte Chemie* 133 (2021): 6049–6058, https://doi.org/10.1002/ange.202014362.

28. F. Liu, X. Lu, C. Shi, and Z. Sun, "Metal-Organic Framework Materials as Bifunctional Electrocatalyst for Rechargeable Zn-Air Batteries," *Batteries & Supercaps* 7 (2024): 202400402, https://doi.org/10.1002/batt.202400402.

29. X. Xu, T. Guo, J. Xia, et al., "Modulation of the crystalline/amorphous interface engineering on Ni-P-O-based catalysts for boosting urea electrolysis at large current densities," *Chemical Engineering Journal* 425 (2021): 130514, https://doi.org/10.1016/j.cej.2021.130514.

30. G. Solomon, R. Mazzaro, S. You, et al., "Ag2S/MoS2 nanocomposites Anchored on Reduced Graphene Oxide: Fast Interfacial Charge Transfer for Hydrogen Evolution Reaction," *ACS Applied Materials & Interfaces* 11 (2019): 22380–22389, https://doi.org/10.1021/acsami.9b05086.

31. S.-K. Park, S.-H. Yu, S. Woo, et al., "A Simple L-cysteine-assisted Method for the Growth of MoS 2 Nanosheets on Carbon Nanotubes for High-performance Lithium Ion Batteries," *Dalton Transactions* 42 (2013): 2399–2405, https://doi.org/10.1039/C2DT32137H.

32. S. Khatun and P. Roy, "Mott-Schottky Heterojunction of Se/NiSe2 as Bifunctional Electrocatalyst for Energy Efficient Hydrogen Production via Urea Assisted Seawater Electrolysis," *Journal of Colloid and Interface Science* 630 (2023): 844–854, https://doi.org/10.1016/j.jcis.2022.10.149.

33. V. Maruthapandian, S. Kumaraguru, S. Mohan, V. Saraswathy, and S. Muralidharan, "An Insight on the Electrocatalytic Mechanistic Study of Pristine Ni MOF (BTC) in Alkaline Medium for Enhanced OER and UOR," *ChemElectroChem* 5 (2018): 2795–2807, https://doi.org/10.1002/celc.201800802.

34. J. Wang, M. Sun, X. Zhang, et al., "pH-Dependent Urea Electrooxidation: From Mechanism to Catalysts and Applications," *Advanced Materials* 38 (2026): 15043, https://doi.org/10.1002/adma.202515043.

35. Y. Li, H. Guo, Y. Zhang, and R. Song, "Cooperative Phosphorus and Chromium Doping Induced Electronic and Morphological Dual Modulation in NiMoO4 Hydrate for Energy-efficient Urea-assisted Hydrogen Production," *Applied Catalysis B: Environmental* 341 (2024): 123296, https://doi.org/10.1016/j.apcatb.2023.123296.

36. L. Sha, T. Liu, K. Ye, et al., "A Heterogeneous Interface on NiS@Ni_3S_2/$NiMoO_4$ Heterostructures for Efficient Urea Electrolysis," *Journal of Materials Chemistry A* 8 (2020): 18055–18063, https://doi.org/10.1039/D0TA04944A.

37. J. Li, J. Li, T. Liu, et al., "Inside Back Cover: Deciphering and Suppressing Over-Oxidized Nitrogen in Nickel-Catalyzed Urea Electrolysis (Angew. Chem. Int. Ed. 51/2021)," *Angewandte Chemie International Edition* 60 (2021): 26867–26867, https://doi.org/10.1002/anie.202114404.

38. X. Zhao, H. Zheng, H. Sun, et al., "Interfacial Component Coupling Effects Induce Electron Redistribution for Enhanced Hydrazine-Assisted Hydrogen Production at Ampere-Level Current Densities," *Nano Energy* 142 (2025): 111201, https://doi.org/10.1016/j.nanoen.2025.111201.

39. J. Zhang, Y. Li, T. Zhu, et al., "3D Coral-Like Ni 3 S 2 on Ni Foam as a Bifunctional Electrocatalyst for Overall Water Splitting," *ACS Applied Materials & Interfaces* 10 (2018): 31330–31339, https://doi.org/10.1021/acsami.8b09361.

40. S. H. Ahn, S. J. Hwang, S. J. Yoo, et al., "Electrodeposited Ni Dendrites With High Activity and Durability for Hydrogen Evolution Reaction in Alkaline Water Electrolysis," *Journal of Materials Chemistry* 22 (2012): 15153, https://doi.org/10.1039/c2jm31439h.

41. M. Gong, D.-Y. Wang, C.-C. Chen, B.-J. Hwang, and H. Dai, "A Mini Review on Nickel-based Electrocatalysts for Alkaline Hydrogen Evolution Reaction," *Nano Research* 9 (2016): 28–46, https://doi.org/10.1007/s12274-015-0965-x.

42. S. V. Chauhan, K. K. Joshi, P. M. Pataniya, and C. Sumesh, "Advancing Industrial Rate Current Density in Water Electrolysis for Green Hydrogen Production: Catalyst Development, Benchmarking, and Best Practices," *Sustainable Energy & Fuels* 9 (2025): 3550–3576, https://doi.org/10.1039/D5SE00262A.

43. N. N. Som, A. Opalinska, M. Chandel, et al., "Cutting-edge PCN-ZnO Nanocomposites With Experimental and DFT Insights Into Enhanced Hydrogen Evolution Reaction," *ACS Applied Energy Materials* 7 (2024): 9402–9413, https://doi.org/10.1021/acsaem.4c01932.

44. S. V. Chauhan, K. K. Joshi, P. M. Pataniya, and C. Sumesh, "Catalyst-Anchored 3D Framework Electrodes: A Breakthrough in Large-Scale Hydrogen Production, Particle & Particle Systems," *Characterization* 42 (2025): 2400226.

45. S. V. Chauhan, K. K. Joshi, P. Sahatiya, G. R. Bhadu, and P. M. Pataniya, "2D–2D NiMo-LDH/MXene Hybrid Electrocatalyst for Durable and Efficient Overall Water Splitting at High Current Densities," *Sustainable Energy & Fuels* 10 (2026): 818–833, https://doi.org/10.1039/D5SE01414J.

46. Y. Lu, T. Liu, C. L. Dong, et al., "Tuning the Selective Adsorption Site of Biomass on Co_3O_4 by Ir Single Atoms for Electrosynthesis," *Advanced Materials* 33 (2021): 2007056, https://doi.org/10.1002/adma.202007056.

47. Y. Yang, L. Liu, S. Chen, et al., "Tuning Binding Strength of Multiple Intermediates towards Efficient pH-universal Electrocatalytic Hydrogen Evolution by Mo_8O_{26} -NbN x O y Heterocatalysts," *Angewandte Chemie* 135 (2023): 202306896 , https://doi.org/10.1002/ange.202306896.

48. X. Shen, H. Li, T. Ma, et al., "Construction of Heterojunction-Rich Metal Nitrides Porous Nanosheets Electrocatalyst for Alkaline Water/Seawater Splitting at Large Current Density," *Small* 20 (2024): 2310535, https://doi.org/10.1002/smll.202310535.

49. B. F. Banti, M. Goddati, N. Nwaji, et al., "Defect Engineered Ru-CoMOF@ MoS_2 Heterointerface Facilitate Water Oxidation Process," *ChemSusChem* 18 (2025): 202402533.

50. D. Chen, R. Lu, R. Yu, et al., "Work-function-induced Interfacial Built-in Electric Fields in Os-$OsSe_2$ Heterostructures for Active Acidic and Alkaline Hydrogen Evolution," *Angewandte Chemie International Edition* 61 (2022): 202208642, https://doi.org/10.1002/anie.202208642.

Supporting Information

Additional supporting information can be found online in the Supporting Information section.

Supporting File: smll75303-sup-0001-SuppMat.docx.